Synthetic light-cone catalogues of modern redshift and weak lensing surveys with ABACUSSUMMIT

Boryana Hadzhiyska [1,2,3]★ S. Yuan [3] C. Blake,[4] D. J. Eisenstein [5] J. Aguilar,[1] S. Ahlen,[6]
D. Brooks,[7] T. Claybaugh,[1] A. de la Macorra,[8] P. Doel,[7] N. Emas,[4] J. E. Forero-Romero,[9]
C. Garcia-Quintero,[10] M. Ishak,[10] S. Joudaki,[11] E. Jullo,[12] R. Kehoe,[13] T. Kisner,[1] A. Kremin,[1]
A. Krolewski,[11,14,15] M. Landriau,[1] J. U. Lange,[16] M. Manera,[17] R. Miquel,[17,18] Jundan Nie,[19]
C. Poppett,[1,2,20] A. Porredon,[21,22] G. Rossi,[23] R. Ruggeri,[4,24] C. Saulder,[25] M. Schubnell,[16] G. Tarlé,[16]
B. A. Weaver,[26] E. Xhakaj[27] and Zhimin Zhou[19]

Affiliations are listed at the end of the paper

ABSTRACT

The joint analysis of different cosmological probes, such as galaxy clustering and weak lensing, can potentially yield invaluable insights into the nature of the primordial Universe, dark energy, and dark matter. However, the development of high-fidelity theoretical models is a necessary stepping stone. Here, we present public high-resolution weak lensing maps on the light-cone, generated using the *N*-body simulation suite ABACUSSUMMIT, and accompanying weak lensing mock catalogues, tuned to the Early Data Release small-scale clustering measurements of the Dark Energy Spectroscopic Instrument. Available in this release are maps of the cosmic shear, deflection angle, and convergence fields at source redshifts ranging from $z = 0.15$ to 2.45 as well as cosmic microwave background convergence maps for each of the 25 base-resolution simulations ($L_{box} = 2000\,h^{-1}$ Mpc and $N_{part} = 6912^3$) as well as for the two huge simulations ($L_{box} = 7500\,h^{-1}$ Mpc and $N_{part} = 8640^3$) at the fiducial ABACUSSUMMIT cosmology. The pixel resolution of each map is 0.21 arcmin, corresponding to a HEALPIX N_{side} of 16 384. The sky coverage of the base simulations is an octant until $z \approx 0.8$ (decreasing to about 1800 deg^2 at $z \approx 2.4$), whereas the huge simulations offer full-sky coverage until $z \approx 2.2$. Mock lensing source catalogues are sampled matching the ensemble properties of the Kilo-Degree Survey, Dark Energy Survey, and Hyper Suprime-Cam data sets. The mock catalogues are validated against theoretical predictions for various clustering and lensing statistics, such as correlation multipoles, galaxy–shear, and shear–shear, showing excellent agreement. All products can be downloaded via a Globus endpoint (see Data Availability section).

Key words: gravitational lensing: weak – methods: numerical – galaxies: haloes – cosmic background radiation – large-scale structure of Universe.

1 INTRODUCTION

The quest to test the standard model of cosmology and pin down possible deviations from it has spawned a number of large-scale structure (LSS) experiments. Measuring the statistics of LSS provides a powerful tool for constraining dark energy, which complements Type Ia supernovae and cosmic microwave background (CMB) probes. The galaxy two-point correlation function, which describes the spatial clustering of galaxies, has provided some of the earliest and most robust evidence for the ΛCDM model (Groth & Peebles 1977; Blumenthal et al. 1984; Maddox et al. 1990; Collins, Nichol & Lumsden 1992; Baugh 1996; Maddox, Efstathiou & Sutherland 1996; Szapudi & Gaztanaga 1998; Saunders et al. 2000; Eisenstein & Zaldarriaga 2001; Huterer, Knox & Nichol 2001; Percival et al. 2001; Hamilton & Tegmark 2002; Cole et al. 2005; Tegmark et al. 2006; Padmanabhan et al. 2007). In addition, LSS is sensitive to dark

matter and dark energy through cosmic shear – slight distortions of the shapes of background galaxies due to the gravitational lensing of the light rays travelling towards us. A benefit of cosmic shear measurements is that they are more directly related to the distribution of mass and can thus be used to stress test the cosmological paradigm. Finally, the cross-correlation between lens galaxy positions and source galaxy shapes, known as galaxy–galaxy lensing, provides a link between galaxy clustering and cosmic shear and a powerful tool for the joint analysis of weak lensing and galaxy clustering measurements, which is known to break degeneracies between a number of model parameters, thereby harvesting more constraining power for the cosmological parameters (Brainerd, Blandford & Smail 1996; Fischer et al. 2000; Mandelbaum et al. 2006, 2013; Johnston et al. 2007; Cacciato et al. 2009; Choi et al. 2012; Leauthaud et al. 2012, 2017; Velander et al. 2014; Clampitt et al. 2017; Kwan et al. 2017; Prat et al. 2018). The combination of these LSS probes – galaxy clustering, cosmic shear, and galaxy-galaxy lensing – informs us about both structure formation in the late Universe and helps us calibrate poorly understood astrophysical processes.

★ E-mail: boryanah@alumni.princeton.edu

To meet the science goals of the new generation of surveys (DESI, *Euclid*, DES, KiDS, HSC, *LSST*) (LSST Dark Energy Science Collaboration 2012; Amendola et al. 2013; Flaugher et al. 2015; Kuijken et al. 2015; Dark Energy Survey Collaboration 2016; DESI Collaboration 2016a; Abbott et al. 2018; Aihara et al. 2018; Hikage et al. 2019; Levi et al. 2019; Heymans et al. 2021), it is crucial to match our experimental efforts with theoretical ones. However, the lensing correlations on subdegree angular scales are the result of non-linear gravitational clustering, which cannot be described by a purely analytical prescription. In lieu of a completely analytical model, cosmologists often adopt numerical *N*-body simulations, which through clever computational techniques, arrive at the answer for the non-linear growth of LSSs, and can thus be used to model the gravitational lensing distortions. Traditionally, producing weak lensing observables via numerical simulations relies on ray-tracing techniques (Blandford et al. 1991; Wambsganss, Cen & Ostriker 1998; Jain, Seljak & White 2000; White & Hu 2000; Hamana et al. 2002; Vale & White 2003; White & Vale 2004; Hilbert et al. 2009; Becker 2013). In this approach, light rays are back-traced from the observer to the source, as they are deflected from multiple projected-mass lens planes. Statistics measured from ray-tracing simulations have shown good agreement with the predictions of non-linear theory, but they come at a substantial computational price and are thus often restricted to small (few deg^2) patches in the sky.

In order to accurately model the wide-field measurements of current experiments, one needs to cover a wide range of scales: from the few-degree large linear scales down to the few-arcmin small non-linear scales. An alternative method to ray-tracing, which is much less computationally expensive and thus readily capable of producing large lensing maps, involves the so-called Born approximation, where the matter from an *N*-body simulation is projected along unperturbed paths using the single-plane approximation. This method can be implemented over large-volume high-resolution simulations and is well-known to yield accurate weak lensing observables on the curved sky for sources at $z_s \sim 3$ or the CMB lensing (for $z_s \approx 1100$) (Gaztanaga & Bernardeau 1998; Das & Bode 2008; Fosalba et al. 2008; Teyssier et al. 2009).

Apart from the method of producing weak lensing maps, one needs to also decide on a 'galaxy-painting' technique for generating mock catalogues with realistic galaxy populations in an *N*-body simulation. Several well-known galaxy population mechanisms are often adopted: the halo occupation distribution (HOD; e.g. Peacock & Smith 2000; Seljak 2000; Scoccimarro et al. 2001; Berlind & Weinberg 2002; Kravtsov et al. 2004; Zheng et al. 2005), which describes the probability a halo with mass M_{halo} contains N_g galaxies; subhalo abundance matching (SHAM; e.g. Vale & Ostriker 2004; Conroy, Wechsler & Kravtsov 2007), which relates directly subhalo properties (such as mass and circular velocity) to galaxy properties (such as luminosity and stellar mass); and semi-analytical models (SAMs; e.g. Baugh 2006; Somerville et al. 2008; Benson 2012), which uses analytical prescriptions to model the formation and evolution of galaxies by usually utilizing the halo merger histories. A prerequisite for both SAMs and SHAM models is the existence of subhalo catalogues (as well as well-resolved merger trees in the case of SAMs), which can be challenging to obtain in $\sim$Gpc^3 volume simulations due to the large memory and CPU requirements needed to output them. Recent advances in HOD modelling (see e.g. Hadzhiyska et al. 2020, 2021a; Xu, Zehavi & Contreras 2021a; Xu et al. 2021b; Yuan et al. 2022) allowing for greater flexibility and accuracy of the model have recast the HOD method into a favoured choice for efficiently populating cosmological volume simulations with galaxies in the era of large redshift surveys.

Here, we employ the ABACUSSUMMIT suite of high-performance cosmological *N*-body simulations (Maksimova et al. 2021b), designed to meet the simulation requirements of the Dark Energy Spectroscopic Instrument (DESI) survey and run with the high-accuracy cosmological code ABACUS (Garrison et al. 2018, 2021; Garrison, Eisenstein & Pinto 2019). In particular, we populate its halo light-cone catalogues, which have been shown to be accurate at the subper cent level (Hadzhiyska et al. 2022) with galaxies according to the ABACUSHOD model, which equips the baseline HOD model with various generalizations pertaining to halo-scale physics and assembly bias (Yuan et al. 2022).

In this paper, we describe the ABACUSSUMMIT weak lensing products, which consist of octant and all-sky lensing maps with subarcmin resolution as well as source and lens galaxy mock catalogues necessary for simulating cross-correlations between the galaxy and lensing fields. We detail the construction process of the convergence, shear, and deflection field maps as well as the assignment procedure of various synthetic lensing properties to the HOD galaxy mock samples. We validate these observables using basic lensing statistics, such as the convergence angular power spectrum and the shear two-point correlation function, and the cross-correlations of foreground and background galaxy samples. Several similar efforts for generating synthetic weak lensing observables exist in the literature. The Buzzard suite of weak lensing mocks (DeRose et al. 2019) are similar to our work, but instead of the Born approximation, they adopt a ray-tracing technique, which allows one to use lower resolution simulations. We note that the Buzzard mocks cover a smaller area on the sky and have lower resolution than ABACUSSUMMIT, though the ADDGALS technique allows for the injection of a high-density galaxy sample at arbitrary redshifts. Another notable effort in the realm of synthetic lensing catalogues is the CosmoDC2 suite of mocks (Korytov et al. 2019), which is run on a single, but larger box and employs a ray-tracing recipe (output at $N_{side} = 4096$). As a result, the generated patches are smaller but probe deeper redshifts ($z \approx 3$). A benefit of these mocks is that in addition to the lensing properties, they also output stellar mass, morphology, spectral energy distributions, and broad-band filter magnitudes via a semi-analytical prescription. We also highlight the Stage-III-oriented CosmoGridV1 synthetic maps (Kacprzak et al. 2023), which are applied to a variety of cosmologies and adopt the Born approximation. Due to the computational expense, they utilize lower resolution and smaller simulations, and address box repetition issues via a novel shell permutation scheme. Planned for the near future is the generation of ABACUSSUMMIT weak lensing catalogues on the extended cosmology grid, which similarly to the CosmoGridV1 mocks, will be enhanced by baryonification recipes and used to constrain cosmological parameters from Stage-IV survey data. Recently, the MillenniumTNG team released high-fidelity weak lensing maps generated from a full-physics hydrodynamical simulation adopting the Born approximation (Ferlito et al. 2023). Other simulations focusing on weak lensing statistics derived via full ray-tracing include Takahashi et al. (2017) and Harnois-Déraps et al. (2018).

This paper is organized as follows: Section 2 briefly introduces the ABACUSSUMMIT suite of simulations and accompanying products relevant to this study. In Section 3, we explain our procedure for generating weak lensing maps from the dark matter outputs on the light-cone, and validate the products. Section 4 details and tests our recipe for assigning lensing properties to mock galaxies by using two-point shear auto and cross-correlation statistics in harmonic and configuration space. In Section 5, we describe our pipeline for generating realistic DESI-, DES-, HSC-, and KiDS-like mock

catalogues. Finally, in Section 6, we summarize our main results and conclusions.

2 SIMULATIONS

In this section, we introduce the ABACUSSUMMIT suite of high-performance cosmological *N*-body simulations and its relevant components, which were employed in the generation of the ABACUSSUMMIT weak lensing maps and catalogues. ABACUSSUMMIT (Maksimova et al. 2021a) was designed to meet and exceed the Cosmological Simulation Requirements of the DESI survey. The simulations were run with ABACUS (Garrison et al. 2019, 2021), a high-accuracy cosmological *N*-body simulation code, optimized for GPU architectures and for large-volume simulations, on the Summit supercomputer at the Oak Ridge Leadership Computing Facility.

The majority of the ABACUSSUMMIT simulations are made up of the so-called `base` resolution boxes, which house 6912^3 particles in a 2 Gpc h^{-1} box, each with a mass of $M_{\rm part} = 2.1 \ 10^9 \ h^{-1} \, {\rm M}_\odot$. Additionally, we utilize the `huge` boxes with corresponding dimensions of 8640^3 particles in a 7.5 Gpc h^{-1} box (with particle mass of $M_{\rm part} = 5.6 \ 10^{10} \ h^{-1} \, {\rm M}_\odot$). While the ABACUSSUMMIT suite spans a wide range of cosmologies, here we focus on the fiducial outputs ($\Omega_{\rm b} h^2 = 0.02237$, $\Omega_{\rm c} h^2 = 0.12$, $h = 0.6736$, $10^9 A_s = 2.0830$, $n_{\rm s} = 0.9649$, $w_0 = -1$, $w_a = 0$), consisting of 25 `base` (AbacusSummit_base_c000_ph{000-024}) and two `huge` runs (AbacusSummit_huge_c000_ph{201,202}). For full details on all data products, see Maksimova et al. (2021a).

2.1 Particle light-cone catalogues

ABACUSSUMMIT outputs a number of light-cone quantities. At every time-step, ABACUS identifies particles that belong to the light-cone and outputs their positions, velocities, particle IDs, and HEALPIX pixel number. The particle outputs contain only a 10 per cent subsample of the particles, the so-called A and B subsamples, whereas the HEALPIX products contain all particles. The pixel orientation of the latter is such that the $+z$ direction coincides with the North Pole. These maps come at a resolution of $N_{\rm side} = 16\,384$, corresponding to ∼0.2 arcmin, sufficient to probe the subhalo regime.

The geometrical arrangement of the `base` light-cones is shown in Fig. 1. In these simulations, which have box length of 2 h^{-1} Gpc on a side, the light-cone observer is positioned at $(-990, -990, -990)$, or, in other words, 10 h^{-1} Mpc inside the corner of the original box. Three boxes, seamlessly attached to each other in an L shape, form the eligible space of the light-cone, centred at $(0, 0, 0)$, $(0, 0, 2000)$, and $(0, 2000, 0)$, respectively (measured in h^{-1} Mpc units). Particles are output on-the-fly from every time-step, where their trajectories are linearly interpolated to find the time when the light-cone intersects their paths. Their positions and velocities are updated to this time. This provides an octant to a distance of 1990 h^{-1} Mpc ($z \approx 0.8$), shrinking to two patches each about 900 square degrees at a distance of 3990 h^{-1} Mpc ($z \approx 2.45$). We stress that all structure below $z \approx 0.8$ comes from the original box and is thus 'unique', while at higher redshifts, the repeated (overlapping) volume between the copies is minimal. In the case of the `huge` box simulations, the light-cone is simply one copy of the box, centred at $(0, 0, 0)$, providing a full-sky light-cone to the half-distance of the box (3.75 Gpc h^{-1}, $z \approx 2.18$), which shrinks as one pushes further towards the eight corners (e.g. half the sky at $z = 3.2$).
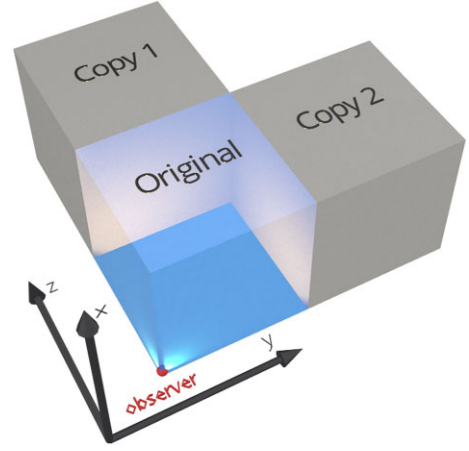

Figure 1. Visualization of the geometrical arrangement of the ABACUSSUMMIT light-cones. The original box, of length 2 h^{-1} Gpc, is centred at (0, 0, 0), while two identical copies are placed at (0, 0, 2000) and (0, 2000, 0) h^{-1} Mpc. The observer is located at the corner of the original box, at $(-990, -990, -990)$ h^{-1} Mpc.

2.2 Halo light-cone catalogues

The halo light-cones of ABACUSSUMMIT provide an accurate and efficient mechanism for obtaining realistic galaxy catalogues on the sky via simulations, which is crucial for testing out systematic and observational effects, and developing pipelines for novel summary statistics.

The procedure for obtaining the ABACUSSUMMIT halo catalogues, introduced in Hadzhiyska et al. (2022), starts with the ABACUSSUMMIT merger trees (Bose et al. 2022), from which we calculate the interpolated positions and velocities of each halo at the redshift at which they cross the observer's light-cone. We then associate the particles belonging to these haloes with the particle light-cone outputs and report a number of new halo properties, in addition to the standard ones, such as merger-tree-interpolated and particle-averaged positions and velocities as well as interpolated masses. The thus obtained halo catalogues can then be populated with galaxies using the ABACUSHOD prescription, which we describe next. We recommend using the halo light-cone products in the halo mass regime of $M_{\rm halo} \gtrsim 2 \times 10^{11} \ h^{-1} \, {\rm M}_\odot$, corresponding to haloes containing ∼100 particles or more, as at these mass scales the merger tree information is available to the vast majority of haloes and the particle-averaged quantities are less noisy. The `base` catalogues are generated for the redshift epochs: $z = 0.1, 0.15, 0.2, 0.25, 0.3, 0.35, 0.4, 0.45, 0.5, 0.575, 0.65, 0.725, 0.8, 0.875, 0.95, 1.025, 1.1, 1.175, 1.25, 1.325, 1.4, 1.475, 1.55, 1.625, 1.7, 1.775, 1.85, 1.925, 2.0, 2.25,$ and 2.5. The `huge` catalogues are available for all the same epochs until $z = 2.25$. The ABACUSSUMMIT halo light-cone catalogues are available at DOI:10.13139/OLCF/1825069.

2.3 ABACUSHOD

The ABACUSSUMMIT halo light-cone catalogues are designed to generate mock catalogues via ABACUSHOD, a sophisticated routine that builds upon the baseline HOD model by incorporating various extensions affecting both the so-called one- and two-halo terms.

ABACUSHOD allows the user to specify different tracer types: emission-line galaxies (ELGs), luminous red galaxies (LRGs), and quasi-stellar objects (QSOs). The ABACUSHOD model is described in detail in Yuan et al. (2022).

The baseline HOD for LRGs comes from the five-parameter model described in Zheng et al. (2005), which gives the mean expected number of central and satellite galaxies per halo given halo mass:

$$\bar{n}_{\rm cent}^{\rm LRG}(M) = \frac{1}{2}{\rm erfc}\left[\frac{\log_{10}(M_{\rm cut}/M)}{\sqrt{2}\sigma}\right], \qquad (1)$$

$$\bar{n}_{\rm sat}^{\rm LRG}(M) = \left[\frac{M - \kappa M_{\rm cut}}{M_1}\right]^{\alpha} \bar{n}_{\rm cent}^{\rm LRG}(M), \qquad (2)$$

where the five parameters describing the model are $M_{\rm cut}$, M_1, σ, α, and κ. $M_{\rm cut}$ characterizes the minimum halo mass to host a central galaxy. M_1 characterizes the typical halo mass that hosts one satellite galaxy. σ describes the steepness of the transition from 0 to 1 in the number of central galaxies. α is the power-law index on the number of satellite galaxies. $\kappa M_{\rm cut}$ gives the minimum halo mass to host a satellite galaxy.

Similarly, the baseline HOD for ELGs is based on the parametric model described in Alam et al. (2020):

$$\bar{n}_{\rm cent}^{\rm ELG}(M) = 2A\phi(M)\Phi(\gamma M)$$
$$+ \frac{1}{2Q}\left[1 + {\rm erf}\left(\frac{\log_{10} M_h - \log_{10} M_{\rm cut}}{0.01}\right)\right], \qquad (3)$$

where

$$\phi(x) = \mathcal{N}(\log_{10} M_{\rm cut}, \sigma_M), \qquad (4)$$

$$\Phi(x) = \int_{-\infty}^{x} \phi(t)\,dt = \frac{1}{2}\left[1 + {\rm erf}\left(\frac{x}{\sqrt{2}}\right)\right], \qquad (5)$$

$$A = p_{\rm max} - 1/Q. \qquad (6)$$

The satellite occupation adopts the same form as equation (2). This baseline HOD form for ELGs is also confirmed in simulation and semi-analytical model approaches by studies such as Hadzhiyska et al. (2021b) and Gonzalez-Perez et al. (2020).

The ABACUSHOD model incorporates several additional decorations beyond the vanilla HOD prescription. Below, we list the most relevant ones:

(i) s is the satellite profile modulation parameter, which modulates how the radial distribution of satellite galaxies within haloes deviate from the radial profile of the halo.

(ii) α_c and α_s are the central and satellite velocity bias parameters, which modulate the peculiar velocity of the galaxies.

(iii) A_c and A_s are the concentration assembly bias parameters for centrals and satellites, respectively.

(iv) B_c and B_s are the environment assembly bias parameters for centrals and satellites, respectively. To define halo environment, we adopt the same formalism as Hadzhiyska et al. (2020).

(v) δM_1, α_1, and β are parameterers specifying the central–satellite and satellite–satellite conformity of the ELGs, which has been found to affect non-trivially the one-halo term behaviour of star-forming galaxies (see e.g. Jiménez et al. 2019; Hadzhiyska et al. 2023b).

We note that the assembly bias implementation preserves the overall galaxy number density by reranking haloes based on their pseudo-mass.

To emulate the intrinsic redshift-dependent change in the galaxy population, we implement a simple redshift-dependent HOD, which linearly (in scale factor, a) interpolates between the best-fitting HOD values at a pair of redshifts for each tracer. The redshift-evolved value of parameter μ takes the following form (for a list of the parameters for each tracer, see Table 1):

$$\mu_i(z) = \mu_{i,0} + \mu_{i,p}\left(\frac{1}{1+z} - \frac{1}{1+z_{\rm pivot}}\right), \qquad (7)$$

where $\mu_{i,0}$ and $\mu_{i,p}$ are the parameter value and its derivative computed at some redshift given two reference points, and i iterates over all free parameters in the model. The values of the HOD parameters we adopt are discussed next.

2.4 Galaxy samples

The main propellant of this work is the need to create accurate weak lensing catalogues in anticipation of planned joint studies between the DESI redshift survey and photometric surveys (e.g. HSC, DES, and KiDS) that measure the induced shapes of galaxies by the effect of gravitational lensing.

2.4.1 DESI

DESI is a Stage-IV dark energy experiment currently conducting a 5-yr survey of about a third of the sky with the goal to amass spectra for approximately 40 million galaxies and quasars (DESI Collaboration 2016a). The instrument operates on the Mayall 4-m telescope at Kitt Peak National Observatory (DESI Collaboration 2022) and can obtain simultaneous spectra of almost 5000 objects over a ∼3° field (DESI Collaboration 2016b; Silber et al. 2023) thanks to a robotic, fibre-fed, highly multiplexed spectroscopic surveyor. The goal of the experiment is to unravel the nature of dark energy through precise measurements of the expansion history (Levi et al. 2013) and thus the dark energy equation of state parameters w_0 and w_a, with a predicted factor of 5–10 improvement on their error relative to previous Stage-III experiments (DESI Collaboration 2016a).

To obtain the HOD parameters of our DESI-like LRG and ELG samples, we fit the predicted three-dimensional correlations to the measured full-shape clustering on small scales ($r \lesssim 30\,h^{-1}$ Mpc) from the DESI SV3 (Survey Validation 3) data. The fits are performed using the dynamic nested sampling package, DYNESTY, on the cubic base-resolution boxes. DYNESTY chains are run separately for each tracer and redshift epoch with covariance matrices computed from the ∼1800 small ABACUSSUMMIT boxes (a set of simulations with base mass resolution, containing 1728^3 particles in a $0.5\,h^{-1}$ Gpc box.), designed with the express purpose of calculating covariance matrices for different summary statistics. The parameter values we arrive at are shown in Table 1 (Yuan & DESI Collaboration 2023).

In the case of our lensing mocks, we take the best-fitting values at redshifts $z = \{0.5, 0.8\}$ for the LRGs and $z = \{0.8, 1.1\}$ for the ELGs without perturbing their values. Assuming that these parameters evolve linearly with the scale factor a, we then calculate the parameter values at each redshift epoch of interest. The minimum and maximum values each parameter can take are set by the prior used in the fitting (see Yuan & DESI Collaboration 2023). That way we avoid adopting unphysical values for our HOD. The redshifts over which the HODs are applied to both LRGs and ELGs span between $z = 0.3$ and $z = 1.4$. These are chosen to roughly cover the range for which the target selection of the tracers is considered robust and the relative number density of the galaxies is large.

2.4.2 HSC, DES, KiDS

For the mock galaxy catalogues of the weak lensing surveys, rather than applying an HOD, we make use of the ABACUSSUMMIT halo light-cone catalogues, selecting all haloes above a minimum mass

Table 1. ABACUSHOD parameters adopted for the DESI GQC galaxy mock catalogues. The redshift-evolving HOD parameters of the lensing mocks are obtained by linearly interpolating the parameters in the table between $z = 0.3$ and $z = 1.4$. Parameters come from the best fits to the DESI early data release. The quenching parameter Q in the central ELG occupation is fixed to $Q = 100$.

Tracer	z	p_{max}	$\log(M_{cut})$	κ	σ	$\log(M_1)$	α	γ	α_c	α_s	A_s	δM_1	α_1	β	B_{cen}	B_{sat}	s
ELG	1.1	0.156	11.65	8.98	2.47	15.32	1.29	5.08	0.0173	0.20	0.11	-1.70	-2.99	9.94	–	–	–
ELG	0.8	0.116	11.52	3.58	1.18	15.97	1.29	4.04	0.180	0.523	0.289	-2.54	-2.59	6.77	–	–	–
LRG	0.8	–	12.65	0.246	0.081	14.00	1.19	–	0.165	0.943	–	–	–	–	0.117	-0.921	0.124
LRG	0.5	–	12.77	0.396	0.060	13.92	1.36	–	0.308	0.913	–	–	–	–	0.063	-0.206	0.481

cut to match the required source number density at each redshift (see Section 5.1 for more details). The reason we opt for this rather simplistic scheme is that in this study, we are not interested in modelling the clustering of the sources but rather only their cross-correlation with the lens sample, which is largely insensitive to the particular choice of a source population model because the measurement depends only on the quality of the shapes and the source number density (Mandelbaum 2018). We note that since we only use haloes for our sources, the source mock catalogues as such are unsuitable for estimating highly non-linear-scale effects such as boost factors and clustering redshifts. However, generating an alternative source galaxy sample on the light-cone using ABACUSHOD and equipping it with weak lensing properties (i.e. shears and deflections) is trivial, and our pipeline and products provide the necessary machinery for doing that.

3 WEAK LENSING MAPS

Matching the halo light-cone catalogues, we generate weak lensing maps for the 25 `base` boxes (`AbacusSummit_base_c000_ph{000-024}`) and the two `huge` boxes (`AbacusSummit_huge_c000_ph{201,202}`) at the fiducial ABACUSSUMMIT cosmology. We retain the native resolution of the HEALPIX shell outputs on the light-cone, i.e. $N_{side} = 16\,384$, corresponding to a pixel size of 0.21 arcmin. We note that the pixel size is thus larger than the force softening scale of ABACUSSUMMIT, 7.2 kpc h^{-1} (proper), at all available redshifts ($z > 0.15$), so we should not expect the lensing observables to be affected.

As detailed in this section, we compute the lensing observables by weighting the shells by the appropriate lensing kernels, adopting the so-called Onion Universe approach (Fosalba et al. 2015), which assumes the Born approximation. We note that the particle counts shells are generated on-the-fly for each ABACUS time-step, of which there are $\gtrsim 1000$ per simulation. Thus, these shells are output with excellent time granularity of $\Delta\log(a) \sim 0.001$ ($\lesssim 10\,h^{-1}$ Mpc) at the relevant redshifts, so we expect the Born approximation to hold with sufficient accuracy for our configuration. Maps of the lensing observables – convergence, shear, and deflection field – are available at 48 source redshifts, covering a redshift range of $z = 0.15$ to $z = 2.4$ ($\Delta z = 0.05$) as well as at the redshift of recombination, $z_{rec} \approx 1089.3$. The geometry of the weak lensing maps is the same as the rest of the light-cone products (see Fig. 1 and the discussion in Section 2.1). To perform the harmonic space operations, we employ the HEALPY and DUCC packages. Comparisons with theory are accomplished via the Cosmological Core Library, PYCCL package.

All products are publicly available at app.globus.org.

3.1 Convergence

To obtain the convergence maps from the particle light-cones, we adopt the Born approximation. Assuming flat space, the convergence field of the lensing distortions is given by

$$\kappa(\theta) = \frac{3H_0^2 \Omega_m}{2c^2} \int d\chi \, \delta(\chi, \theta) \frac{(\chi_s - \chi)\chi}{\chi_s \, a}, \tag{8}$$

where $H_0 = 100h$ km s^{-1} Mpc^{-1} is the Hubble constant, Ω_m is the energy density of matter, c is the speed of light, δ is the three-dimensional matter overdensity at radial distance $\chi(a)$, a is the scale factor, θ is the angular position, and χ_s is the distance to the lensing source(s). Throughout the paper, we use comoving distances in units of h^{-1} Mpc.

In order to compute the convergence map in an N-body simulation by adding up the light-cone shells weighted by the appropriate weak lensing kernel at each redshift, we can discretize this equation as follows (Fosalba et al. 2008):

$$\kappa(i) = \frac{3H_0^2 \Omega_{cb}}{2c^2} \sum_j \delta(ij) \frac{(\chi_s - \chi_j)\chi_j}{\chi_s a_j} \, d\chi_j, \tag{9}$$

where i indicates the pixel position in the sky and j the radial bin index (i.e. distance to the mid-point χ_j[1] and the width $d\chi_j$ of the shell j) into which we have sliced the simulation. Note that since ABACUSSUMMIT uses a basic prescription for neutrinos, modelling them as a smooth, non-clustering matter component (Maksimova et al. 2021a), we need to consider the contribution only from the gravitational components, i.e. baryons and cold dark matter, $\Omega_{cb} = \Omega_b + \Omega_c$. Such a treatment of neutrinos captures accurately the suppression on small scales, but does not account for the neutrino clustering on large scales. However, this is a secondary effect and does not matter for most applications relevant for galaxy surveys.

We can compute the overdensity as

$$\delta(ij) = \frac{\rho(ij)}{\bar{\rho}} - 1, \tag{10}$$

where $\bar{\rho} = \langle\rho(ij)\rangle$ is the mean density, which we compute analytically as (N_{part}/L_{box}^3), and the density per pixel is

$$\rho(ij) = \frac{N_{ij}}{dV_j} = \frac{N_{ij}}{\Delta\Omega \, \chi_j^2 \, d\chi_j}, \tag{11}$$

where $\Delta\Omega$ is the area of each pixel and N_{ij} is the number of particles in pixel i and slice (or equivalently, shell) j. In Fig. 2, we show the convergence map at two source redshifts, $z_s = 1$ and 1089.3, for the `huge`-resolution simulation, `AbacusSummit_huge_c000_201`, which covers the full sky.

---

[1]Note that the field reported in the ABACUSSUMMIT light-cone files, `CoordinateDistanceHMpc`, refers to the distance to the outer edge of the shell.
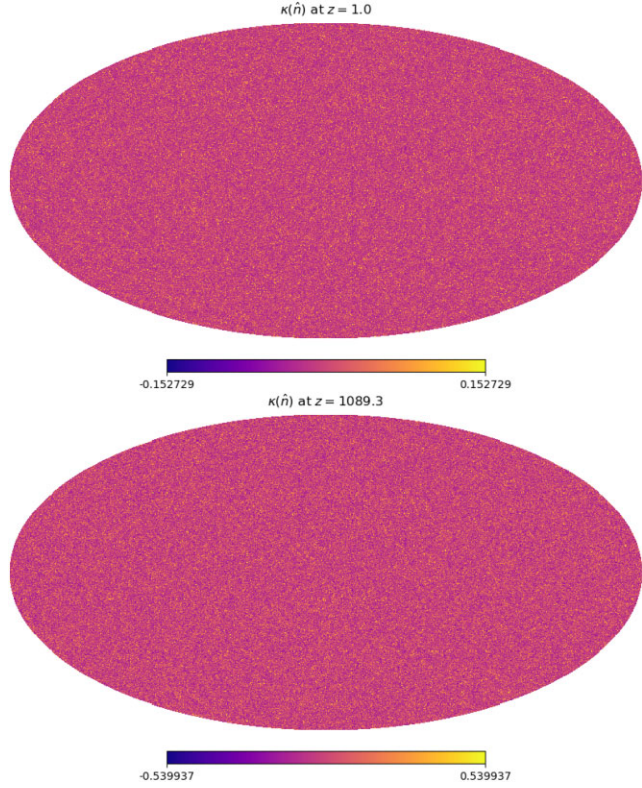
Figure 2. Convergence field at source redshift, z_s, of 1 (top panel) and 1089.3 (bottom panel), corresponding to the epoch of recombination. Maps shown for the `AbacusSummit_huge_c000_ph201` simulation, which places the observer at (0, 0, 0) and thus covers the full sky until $z = 2.18$.

The convergence field, κ, is related to the lensing potential through the two-dimensional Poisson equation,

$$\kappa(\hat{n}) = \nabla^2 \phi(\hat{n}) \tag{12}$$

where $\phi(\hat{n})$ is the lensing potential at a given point on sky, $\hat{n}$. In harmonic space, this equation is greatly simplified, and the coefficients of the spherical harmonic transform, $\kappa(\hat{n}) = \sum_{\ell,m} \kappa_{\ell m} Y_{\ell m}(\hat{n})$, are given by

$$\kappa_{\ell m} = -\frac{1}{2}\ell(\ell+1)\phi_{\ell m}. \tag{13}$$

Thus, at each source plane, we can compute the lensing potential from the convergence map by applying the appropriate ℓ weights in harmonic space. Similarly, thanks to their simple relations to the lensing potential in harmonic space, we can obtain other lensing observables.

3.2 Deflection angle

The deflection angle is related to the lensing potential through its gradient (Hu 2000)

$$\alpha(\hat{n}) = \nabla\phi(\hat{n}). \tag{14}$$

In harmonic space, its coefficients are given by

$$\alpha_{\ell m} = -\sqrt{\ell(\ell+1)}\phi_{\ell m}. \tag{15}$$

Similarly, we can relate the deflection angle to the convergence field as

$$\alpha_{\ell m} = \frac{2}{\sqrt{\ell(\ell+1)}}\kappa_{\ell m}. \tag{16}$$

The corresponding power spectra are thus simply related via $4\,\ell(\ell+1)\,C_\ell^{\alpha\alpha} = C_\ell^{\kappa\kappa}$. To obtain the real-space quantity, we transform back to real space. In HEALPY and DUCC, the default ℓ_{max} when performing the spherical harmonic transform is typically set as $\ell_{max} = 4 \times N_{side}$. However, at $N_{side} = 16\,384$, this constitutes a huge computational expense,[2] so instead we curb it $\ell_{max} = 2 \times N_{side}$ and check via lower resolution maps that this does not affect the power spectrum of the lensing quantity measured at ℓ_{max}.

3.3 Shear

Finally, the shear maps, $\gamma(\hat{n})$, can be related to the convergence field in spherical harmonic space (see Hu 2000) via

$$\gamma_{\ell m} = -\sqrt{(\ell+2)(\ell-1)/(\ell(\ell+1))}\kappa_{\ell m} \equiv -f(\ell)\kappa_{\ell m} \tag{17}$$

and to the lensing potential via

$$\gamma_{\ell m} = \frac{1}{2}f(\ell)\ell(\ell+1)\phi_{\ell m}, \tag{18}$$

with, $f(\ell) = \sqrt{(\ell+2)(\ell-1)/(\ell(\ell+1))}$. Assuming that the B-mode signal is zero for the cosmological weak lensing signal, the shear E-mode harmonic coefficients are given by $E_{\ell m} = \gamma_{\ell m}$, whereas the 'Stokes' parameters of the shear field, γ_1, γ_2, can be obtained by transforming back the $E_{\ell m}$ coefficients to real space:

$$\gamma_1(\hat{n}) \pm i\gamma_2(\hat{n}) = \sum_{\ell m} \gamma_{\ell m} Y_{\ell m}(\hat{n}). \tag{19}$$

Analogously to the case of the deflection field, we set the maximum ℓ-mode of that transformation to $\ell_{max} = 2 \times N_{side}$.

3.4 Validation

Having obtained the convergence maps, we can compare it with the theoretically estimated angular power spectrum from PYCCL (Chisari et al. 2019) given by

$$C_\ell^{\kappa\kappa}(\kappa) = \frac{9H_0^4\Omega_m^2}{4c^4} \int d\chi \, P(k,z)\frac{(\chi_s - \chi)^2}{\chi_s^2\,a^2}, \tag{20}$$

where $P(k, z)$ is the three-dimensional density power spectrum at redshift z evaluated at $k = \ell/\chi$ in the Limber approximation (Limber 1953), which is known to be valid for $\ell > 10$ within a few per cent accuracy (see e.g. Bernardeau et al. 2002).

Fig. 3 shows the comparison between the convergence power spectrum measured from the ABACUSSUMMIT maps and the non-linear theoretical fit (i.e. HALOFIT, as implemented in PYCCL), for sources at $z_s = 1$ and $z_s = 1089.3$. We show the results both for the 25 base-resolution simulations (covering a bit less than an octant at $z_s = 1$ and about 1800 sq. deg at $z_s = 1089.3$) as well as the two huge-resolution simulations (covering the full sky). The theoretical prediction is calculated using PYCCL, which in turn uses the HALOFIT non-linear matter power spectrum. The base-resolution simulation curves demonstrate remarkable agreement with theory for all scales considered ($30 < \ell < 10\,000$). In particular, the CMB lensing agreement is $\lesssim 0.1$ per cent on average, whereas for $z_s = 1$, it is about 1 per cent. We note that the quoted accuracy of HALOFIT is about 5 per cent (Takahashi et al. 2012), so the agreement we observe is far below that threshold. We attribute the worse agreement at $z_s = 1$ between PYCCL and ABACUSSUMMIT to the fact that HALOFIT provides a poorer fit to the simulation power spectrum at low

---
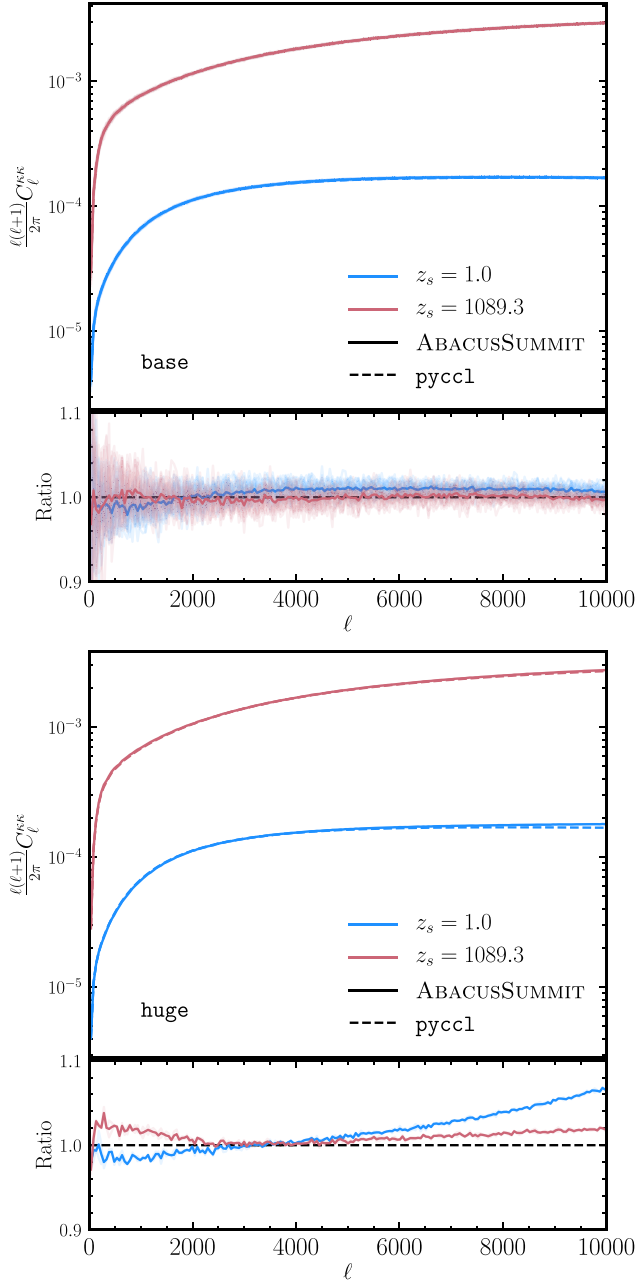
[2]Private correspondence with Martin Reinecke.

Figure 3. Convergence angular power spectrum at two source redshifts, $z_s = 1$ (blue) and $z = 1100$ (red), computed using ABACUSSUMMIT (solid) and the cosmological library PYCCL (dashed). The top panel shows the results for the 25 base-resolution simulations (covering less than an octant), while the bottom is obtained using the two huge-resolution simulations (covering the full sky). Each panel also shows the ratio between the simulation and the theoretical prediction, which is calculated using HALOFIT (total matter). In shaded colours, we plot the curves from all simulations. The simulation curves in the top panel demonstrate remarkable agreement with theory for all scales considered ($30 < \ell < 10\,000$). On smaller scales, cosmic variance contributes to the uncertainty in the measurement. For the huge simulations, the CMB lensing power spectrum deviates at the 2 per cent level with a mild scale dependence, while at $z_s = 1$, the discrepancy reaches 6 per cent. We attribute this difference to resolution effects and further study this in Appendix B.
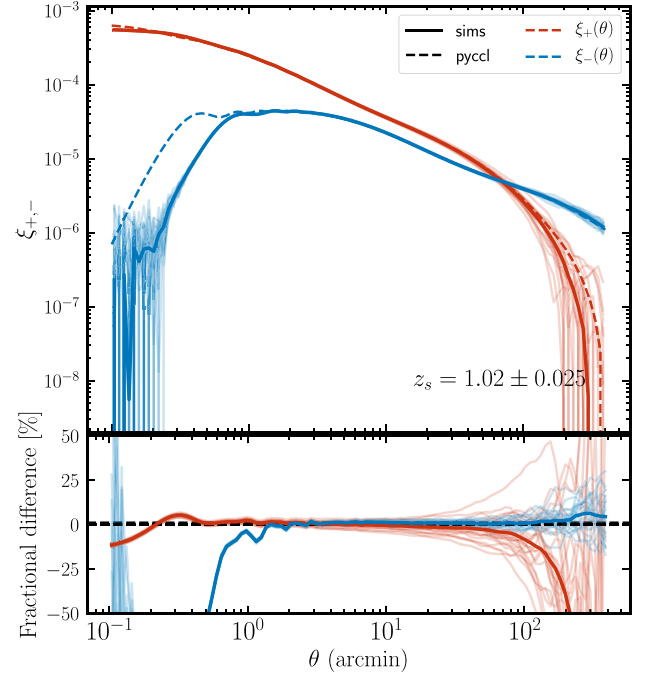

Figure 4. Shear–shear autocorrelation, $\xi_{\pm}(\theta)$, at $z_s = 1.025$ source redshift. Results are shown for all 25 base simulations (shaded), with the average $\xi_{\pm}$ displayed as solid curves (red and blue, respectively). The source catalogue consists of all haloes at that redshift epoch. We find that in the intermediate regime of 1 arcmin $< \theta < 100$ arcmin, the agreement is within 5 per cent. Below 0.7 arcmin, ξ_{-} sees a stark cut-off due to resolution effects coming from the pixel size (0.2 arcmin). Above $\theta = 100$ arcmin, ξ_{+} is more strongly affected by map boundary effects, which are investigated in detail in Appendix A.

redshifts (see Fig. B1 and the commentary in Appendix B). At the lowest multipoles, sample variance introduces large fluctuations in the measured power for a single realization, contributing as much as 10 per cent to the uncertainty in the measurement.

In the case of the huge simulations (shown on the bottom of Fig. 3), we see that the convergence power spectrum is more discrepant with PYCCL. In particular, while the CMB lensing power spectrum deviates at no more than 2 per cent for all scales shown, the deviation is much more evident in the $z_s = 1$ case (and also displays some scale dependence), at the smallest scales reaching 6 per cent. We attribute this difference, relative to the base simulations, to resolution differences. As a separate test, we swap the HALOFIT non-linear power spectrum in PYCCL with Cosmic Emu (Heitmann et al. 2016) and find that the huge simulations' convergence power spectrum is much better matched. We conjecture that this is because Cosmic Emu employs a simulation suite with resolution characteristics that are very similar to the ABACUSSUMMIT huge boxes. Until $\ell < 9000$, the agreement with HALOFIT is within the 5 per cent expected margin. Below $\ell \lesssim 10$, we advise treating the comparisons with caution, as the Limber approximation (adopted in the power spectrum calculation) breaks down (LoVerde & Afshordi 2008).

In Fig. 4, we show the shear–shear autocorrelation, $\xi_{\pm}(\theta)$, at source redshift of $z_s = 1$, computed for all 25 base-resolution simulations. The source catalogue is made up of all the haloes belonging to the source redshift epoch. We find that in the intermediate regime, i.e. 1 arcmin $< \theta < 100$ arcmin, the agreement is within 5 per cent. Below 1 arcmin, $\xi_{+}(\theta)$, which at fixed θ receives contributions from larger

scales relative to $\xi_-(\theta)$ (Schneider et al. 2002), exhibits excellent agreement. On the other hand, we see a steep cut-off in the $\xi_-(\theta)$ curve. This is the result of resolution effects due to the pixel size (0.2 arcmin), which affect $\xi_-(\theta)$ more noticeably than $\xi_+(\theta)$ as argued above. We note that the use of haloes rather than galaxies (particles + haloes) reduces the noise in the $\xi_\pm(\theta)$ measurement. Above $\theta > 100$ arcmin, $\xi_-(\theta)$ displays excellent agreement, whereas $\xi_+(\theta)$ displays a stark cut-off. We conjecture that this is the result of boundary effects in the map construction procedure and investigate this idea in Appendix A through several test on the full-sky huge-resolution box. We conclude that there are two main boundary effects: on one hand, the area covered by the source maps, which is a bit less than an octant at $z_s = 1$, displays significant sample variance at these scales; on the other hand, the conversion of partial-sky $\kappa(\hat{n})$ into $\gamma_{1,2}(\hat{n})$ introduces features at the boundary, which affect the large-scale measurement. We note that at higher redshifts, these effects are more pronounced ($z_s \approx 0.8$ maps cover an octant of the sky, but the area covered shrinks at higher redshifts). Although our correlation measurements exhibit a deficit beyond $\theta > 100$ arcmin, the errors on them are still within the noise of the weak lensing surveys of interest (see Fig. 11, where we mimic DES Y3 with realistic noise) and so have minimal effect on cosmological parameter fits.

4 MOCK CATALOGUES

In this section, we detail our procedure for augmenting our mock galaxies with lensing properties via the weak lensing maps discussed in Section 3.

4.1 Lensing assignment

Mock galaxies are output using the ABACUSHOD method, as discussed in Sections 2.3 and 2.4. To assign lensing properties to each of our mock galaxies, we adopt the following simple algorithm:

(i) For a given galaxy with coordinates on the light-cone $(\hat{n}, z)$, where $\hat{n}$ denotes its angular position in the sky and z its redshift, we find the corresponding closest source plane in redshift and the sky coordinate pixel of the pixels which the galaxy occupies (i.e. discretized pixel centre coordinates)

(ii) Then, we look up the value of the relevant lensing quantities for this pixel and redshift from our convergence and shear weak lensing maps, κ, γ_1, γ_2, as well as the deflection angle values at this location, α_θ and α_ϕ.

(iii) Finally, for each galaxy, we record the values of the weak lensing fields, as well as the perturbed sky coordinates due to the tiny deflection to the light ray caused by gravity (discussed in Section 4.2).

This simple implementation is sensitive to the pixel resolution used, which in our case is 0.21 arcmin ($N_{side} = 16\,384$). Consistently, we only expect to model lensing observables accurately down to ∼0.3 arcmin scales, as we will discuss in detail in Section 5. Another limitation of this procedure is that different galaxies that occupy the same pixel will have identical lensing properties. Given the small physical scale that our choice of N_{side} corresponds to, we expect that this will play a very minor role.

4.2 Magnification bias

The gravitational lensing induced by LSSs on background sources changes their observed number density and thus introduces an additional cross-correlation signal between background and foreground galaxy populations (Moessner & Jain 1998; Bartelmann & Schneider

2001). This effect, first measured in cross-correlations between distant quasars and low-redshift galaxies (e.g. Benítez & Martínez-González 1997; Gaztañaga 2003; Myers et al. 2005; Scranton et al. 2005), is known as 'magnification bias' and can be used to constrain the galaxy–mass power spectrum (Jain, Scranton & Sheth 2003).

To build theoretical intuition, let us consider the case of a magnitude limited survey. Then, the cumulative number of galaxies above a certain flux limit, f, is roughly proportional to $N_0(> f) \propto Af^\alpha$, where A is the area of the survey and α is the power-law slope of the background (source) number counts. Because lensing preserves the surface brightness of galaxies, the observed survey depth increases (i.e. the effective flux limit decreases), whereas the effective area decreases by the same amount: $f \to f/\mu$, $A \to A/\mu$, where μ is the magnification. These two counteracting effects induce a bias in the cumulative number of background sources given by

$$N(> f) \propto \frac{1}{\mu} A \left(\frac{f}{\mu}\right)^{-\alpha} = \mu^{\alpha-1} N_0(> f). \quad (21)$$

In the weak lensing limit, we can approximate the magnification as $\mu \approx 1 + \delta_\mu$ since $|\delta_\mu| \ll 1$. Taylor expanding the magnification term, $\mu^{\alpha-1} \approx 1 + (\alpha-1)\delta_\mu$, we arrive at the following expression for the additional overdensity contributed by the magnification:

$$\delta_{mb} = \frac{N - N_0}{N_0} = \delta_{mm} + \delta_{lp}$$
$$= (\alpha - 1)\delta_\mu = 2(\alpha - 1)\delta_\kappa \quad (22)$$

where the last equality uses the weak lensing approximation that relates the fluctuations in magnification and convergence via $\delta_\mu \approx 2\,\delta_\kappa$. Note that δ_{mb} ('mb' stands for magnification bias) incorporates two qualitatively different contributions:

(i) extra fluctuations from magnified magnitudes, $\delta_{mm} = \alpha\,\delta_\mu$
(ii) extra fluctuations from lensed positions, $\delta_{lp} = -\delta_\mu$.

While the two effects cannot be separated observationally, we implement them in our simulations using two distinct procedures, which are outlined next. We can thus test and verify each one of them separately. Traditionally, we work with the logarithmic slope of the background number counts, s, at redshift z, for a magnitude limit m, defined as

$$s = 2\alpha/5 \equiv \frac{d\text{Log}_{10}N(< m, z)}{dm}. \quad (23)$$

The overall contribution to the counts due to magnification bias thus becomes

$$\delta_{mb} = (5s - 2)\delta_\kappa. \quad (24)$$

The net magnification effect depends on how the loss of sources due to the area contraction, δ_{lp}, is compensated by the gain of sources from the flux magnification, δ_{mm}. Number counts for source populations with flat luminosity functions, $s < 0.4$, such as faint galaxies, decrease due to the effective shrinkage in area, whereas sources with steep luminosity functions, $s > 0.4$, such as quasars, increase due to the effective deepening of the survey. In the case of $s = 0.4$ ($\alpha = 1$), there is no net change to the counts due to magnification bias.

4.3 Implementation of magnification bias

In this section, we describe how we implement magnification in the magnitudes and positions of mock galaxies.

(i) **Magnified magnitudes:** Flux magnification causes the mock galaxy magnitudes, m, to become brighter by the following amount:

$$\Delta m = 2.5 \text{Log}_{10} \mu \approx \frac{5}{\ln 10} \kappa \tag{25}$$

where we have Taylor expanded $\mu \approx 1 + \delta\mu$ and used the weak lensing relation $\delta\mu \approx 2\kappa$ in the weak lensing limit. Knowing the value of the convergence, κ at the location of a given galaxy, we can compute the induced magnification to its flux, which in turn leads to a change in the source number counts, δ_{mm}. In the case of the ABACUSHOD model, we do not output magnitudes or fluxes but only galaxy positions and velocities. For this reason, we implement the effect of magnitude magnification by weighting the galaxies by

$$w = 1 + 2\alpha \, \delta_\kappa = 1 + 5s \, \delta_\kappa, \tag{26}$$

which effectively boosts the contribution of galaxies located at local peaks of the convergence field.

(ii) **Lensed positions:** The observed position of a source galaxy, $\boldsymbol{\beta}$, is shifted from its true (unlensed) position, $\boldsymbol{\theta}$, by an angle determined by the deflection field vector, $\boldsymbol{\alpha}$, at its true location (for details, see Bartelmann & Schneider 2001). In the single-plane (i.e. Born) approximation, the lens equation reads

$$\boldsymbol{\beta} = \boldsymbol{\theta} - \boldsymbol{\alpha} \tag{27}$$

where $\boldsymbol{\alpha}$ is a two-dimensional vector, and the lensed position $\boldsymbol{\beta}$ is obtained by moving the galaxy position along a geodesic on the sphere in the direction of the vector by an amount (arc length) given by the size of the deflection angle, α. Guided by this, we can remap the source galaxy positions due to gravitational lensing in our galaxy outputs.

If we denote the unlensed position on the sphere by $\boldsymbol{\theta} = (\theta, \phi)$, then the lensed position, $\boldsymbol{\beta} = (\theta', \phi + \Delta\phi)$, can be simply written down as

$$\cos\theta' = \cos\alpha \, \cos\theta - \sin\alpha \, \sin\theta \, \cos\delta$$
$$\sin\Delta\phi = \sin\alpha \, \sin\delta / \sin\theta, \tag{28}$$

where we have used the spherical triangle identities (Lewis 2005; Das & Bode 2008) and the deflection vector is projected on the spherical polar basis, $(\mathbf{e}_\theta, \mathbf{e}_\phi)$, as $\boldsymbol{\alpha} = \alpha_\theta \mathbf{e}_\theta + \alpha_\phi \mathbf{e}_\phi = \alpha \cos\delta \, \mathbf{e}_\theta + \alpha \sin\delta \, \mathbf{e}_\phi$, with δ being the angle between the deflection vector and the polar basis vector $\mathbf{e}_\theta$.

In summary, in order to enable magnification bias in the lens catalogues, we recommend calculating the lensed positions of galaxies according to equation (2) and weighting the galaxies by the quantity in equation (28). We adopt the 'lensed positions' for the source catalogue when switching on magnification bias effects, which also affects the sources.

4.4 Validation

4.4.1 Harmonic space

In weak lensing studies, we typically split the data into redshift bins. To obtain the theoretical measure of the angular cross-power spectrum between two fields δ_a, δ_b, measured in redshift bins i, j, we can adopt the following equation:

$$C_{ab}^{ij}(\ell) = \int d\chi \frac{q_a^i(\chi) q_b^j(\chi)}{\chi^2} P_{ab}(\ell/\chi, z(\chi)), \tag{29}$$

where $P_{ab}(k, z)$ is the three-dimensional cross-power spectrum of the fields at redshift z and wavenumber k, $\chi(z)$ is the comoving

distance, and $q_{a, b}(\chi)$ are the weight functions, (Kaiser 1992; Hu & Jain 2004), and we have assumed the Limber approximation (Lemos, Challinor & Efstathiou 2017), $k = \ell/\chi$. For the galaxy density field, δ_g, corresponding to the foreground (lens) galaxy population, the weight function $q_g(\chi)$ is given by

$$q_g^i(\chi) = \frac{n_{\text{lens}}^i(z)}{\bar{n}_{\text{lens}}^i} \frac{dz}{d\chi}, \tag{30}$$

where $n_{\text{lens}}^i(z)$ is the redshift distribution of the sample in redshift bin i and $\bar{n}_{\text{lens}}^i$ is the average lens density. For the convergence field, δ_κ, corresponding to the background (source) galaxy population, the weight function $q_\kappa(\chi)$ can be calculated as

$$q_\kappa^i(\chi) = \frac{3 H_0^2 \Omega_m}{2c^2} \frac{\chi}{a(\chi)} \int_\chi^{\chi_{\max}} d\chi' \frac{n_{\text{source}}^i(z)}{\bar{n}_{\text{source}}^i} \frac{dz}{d\chi'} \frac{(\chi' - \chi)}{\chi'}, \tag{31}$$

where H_0 and Ω_m denote the values of the present-day Hubble parameter and matter density and $\chi_{\max}$ is the maximum comoving distance of the source distribution. Analogously to the lens case, $n_{\text{source}}^i(z)$ and $\bar{n}_{\text{source}}^i$ are the source redshift distribution and average density of sources in redshift bin i. We describe the redshift distributions of our source and lens populations in Section 5.1.

Fig. 5 shows the angular power spectrum of the galaxy–galaxy and galaxy–convergence cross-correlation between two pairs of lens and source galaxy populations; namely, $z_l = 0.5$ ($z_l = 0.8$) and $z_s = 1$ ($z_s = 1.4$) as well as $z_l = 1$ with $z_s = 1100$ for LRGs (ELGs). We choose the pairings in a way that ensures the lens redshift distribution has good overlap with the lensing kernel of the source. We downsample the DESI lens populations of LRGs and ELGs (defined in Section 2.4) to match a Gaussian form of the redshift distribution centred on $z = 0.5$ (0.8) and 1.025, respectively, with a width of $\Delta z = 0.2$. We subtract the Poisson noise contribution from the galaxy clustering signal, but note that the noise term may deviate from the Poisson assumption (e.g. Maleubre et al. 2022). The smallest scales we consider are $\ell = 1000$, as the linear bias approximation worsens as we venture far into the non-linear regime.

At large scales, $\ell < 200$, we see that the agreement with theory of all curves is excellent – i.e. the ratio is consistent with one, within a 10 per cent error budget. Assuming that the scale at which the linear bias approximation breaks down is $k \approx 0.1 \, h \, \text{Mpc}^{-1}$, which corresponds to $\ell \approx 180$ and 300 for $z_l = 0.5$ and 1, respectively (using the Limber approximation), it is no surprise that we start seeing large deviations from the simple HALOFIT + linear bias model around these scales. We note that as expected, the high-redshift pair, which is affected by non-linear physics on smaller scales, follows well the PYCCL prediction down to smaller scales. We choose the linear bias parameters by eye such that they fit the large scales of the galaxy autopower spectrum. The values we arrive at are: 1.1 ($z = 0.8$) and 1.25 ($z = 1.025$) for the ELGs, and 1.95 ($z = 0.5$) and 2.3 ($z = 1.025$) for the LRGs. As will be discussed in the next section (see Figs 6 and 7), relative to the linear bias approximation, the small-scale clustering of ELGs is suppressed while that of LRGs is in excess. Due to the larger size of the LRG haloes, which in turn pushes the effects of the one-halo term to larger scales, it is no surprise that the deviations from the linear bias approximation kick in at smaller values of ℓ. We also observe in the lower (ratio) panels that for a given choice of tracer and redshift, the two curves, $\kappa \times g$ and $g \times g$, divided by their respective linear bias predictions, are in good agreement with each other. This indicates that the galaxy–matter cross-correlation coefficient is close to one. As expected, in the case of the ELGs, the ratios are less consistent with each other, as the cross-correlation coefficient exhibits a larger deviation from one (see e.g. Hadzhiyska et al. 2023a).

Figure 5. Angular power spectrum of the galaxy–galaxy and galaxy–convergence cross-correlation at two source redshifts $z_s = 1$ (1.4) and $z_s \approx 1100$ and two lens redshifts $z_l = 0.5$ (0.8) and $z_l = 1$ for LRGs (ELGs). The top panel corresponds to the LRG galaxy population, while the bottom corresponds to the ELG one. The dotted curves show the Poisson noise contribution to the signal, which we subtract from the $g \times g$ signal. The smallest scales we consider are $\ell < 1000$, as the linear bias approximation worsens, as we plunge into smaller and smaller scales. Similarly to Figs 6 and 7, relative to the linear bias approximation, the small-scale clustering of ELGs is suppressed while that of LRGs is in excess. Results shown for `AbacusSummit_base_c000_ph002`.

4.4.2 Configuration space

When measuring galaxy–galaxy lensing in configuration space, it is convenient to work with the average tangential shear $\langle \gamma_t(\theta) \rangle$, which defines the tangential shear of background galaxies at angular separation θ from a lens galaxy. This quantity is related to the

Figure 6. Galaxy–shear measurement for lens LRG (top) and ELG (middle) samples located at $z_l = 0.5$ and $z_s = 1$ or $z_l = 0.8$ and $z_s = 1.4$, in the case of no magnification bias (solid), lensed positions (dashed), magnified flux (dotted), and both (dash–dotted) (see Section 4.3). Magnification bias has the same response in the simulations (blue) as in theory (red). On large scales, the curves are matched well, but sample variance introduces substantial noise. On small scales, the one-halo term is overpredicted for ELGs and underpredicted for LRGs by the linear bias model. Results are shown for all 25 boxes. The red shaded regions correspond (conservatively) to scales affected by the Born approximation. On the bottom panel, we show the matter–shear measurement computed via our weak lensing mocks (blue), the cubic box (black), and HALOFIT (red), demonstrating excellent agreement down to $\theta \approx 0.4$ arcmin.

convergence κ via $\langle\gamma_t(\theta)\rangle = \langle\overline{\kappa}(<\theta) - \langle\kappa(\theta)\rangle$ with $\overline{\kappa}(<\theta)$ being the integrated convergence within separation θ. Thus, we can express γ_t in terms of the angular cross-power spectrum, $C_\ell^{\kappa g}$, as

$$\gamma_t(\theta) = \int \frac{d\ell\,\ell}{2\pi} C_\ell^{\kappa g} J_2(\ell\theta), \tag{32}$$

where J_2 denotes the second-order Bessel function of the first kind.

In Fig. 6, we show the galaxy–shear cross-correlation measurement for the lens population of LRGs (ELGs) at $z_l = 0.5$ (0.8) and source population at $z_s = 1.025$ (1.4). We adopt the same redshift distribution for the lens population as in Fig. 5, i.e. Gaussian centred at $z = 0.5$ (0.8) with width of $\Delta_z = 0.2$. Additionally, we study the effect of magnification bias by switching on and off the effects of lensed positions and magnified flux, as described in Section 4.3. Qualitatively, the magnification bias curves behave as expected from theory: for our choice of $s = 0.2$ (see Section 4.2), the clustering increases due to flux magnification (effective change of depth) and decreases due to the lensing of the positions (effective change of area). On large scales, the curves are matched well, but sample variance introduces substantial noise at $\theta \gtrsim 100$ arcmin. This echoes our findings in Fig. 4. Similarly to Fig. 5, we see that the one-halo term (and the one-to-two-halo transition) is overpredicted for ELGs and underpredicted for LRGs by the simple HALOFIT model with linear bias. This is the result of the smaller mass (and thus, bias) and lower mean satellite occupation of ELG host haloes, which results in a lower one-halo clustering relative to the two-halo term (which is captured well by modulating the bias). The opposite is true for LRGs, which are hosted by haloes that are larger than the typical halo (and thus, more biased) and on average in the high-mass end, contain many more satellites. We note that the PYCCL predictions use the same values of the bias as Fig. 5; namely, 1.1 ($z = 0.8$) and 1.25 ($z = 1.025$) for the ELGs, and 1.95 ($z = 0.5$) and 2.3 ($z = 1.025$) for the LRGs. We revisit the galaxy lensing measurement in Fig. 12, where we explore the predicted signal for DES Y3 with realistic noise properties.

In the bottom panel of Fig. 6, we show the particle- (matter-)shear measurement obtained from our weak lensing maps (averaging over all 25 simulations), the cubic box (by converting $\Delta_\Sigma(r_p)$ into $\gamma_t(\theta)$ for a single realization, `AbacusSummit_base_c000_ph002`), and the HALOFIT prediction from PYCCL. The three curves show remarkable consistency with each other, which reassures us of the validity of our mocks. Below $\theta \lesssim 0.4$, we begin to see deviations between the weak lensing curve and the HALOFIT prediction, which can be attributed to the breaking down of the Born approximation below scales associated with the root mean square of the deflection angle, α. We note that in this calculation, we use the unlensed positions of both lenses and sources, whereas for the two galaxy panels above, we use the more 'physically correct' lensed positions. However, we expect that in the single-plane (Born) approximation, the angular deflection by which we move the galaxies is not entirely accurate, leading to decorrelations between the matter field and the tracers, and thus a suppression in the measured clustering. The shaded band in the top two panels demarcates the region where we conservatively expect the Born approximation to break down ($\theta < 1$ arcmin).

In order to validate our lens population catalogues, we compute another useful projected galaxy clustering statistic, the standard projected two-point correlation function $w_p(r)$, defined as

$$w_p(r) = \sum_{\pi=0}^{\pi_{\max}} \left[\frac{DD(r,\pi) - 2DR(r,\pi) + RR(r,\pi)}{RR(r,\pi)} - 1 \right], \tag{33}$$
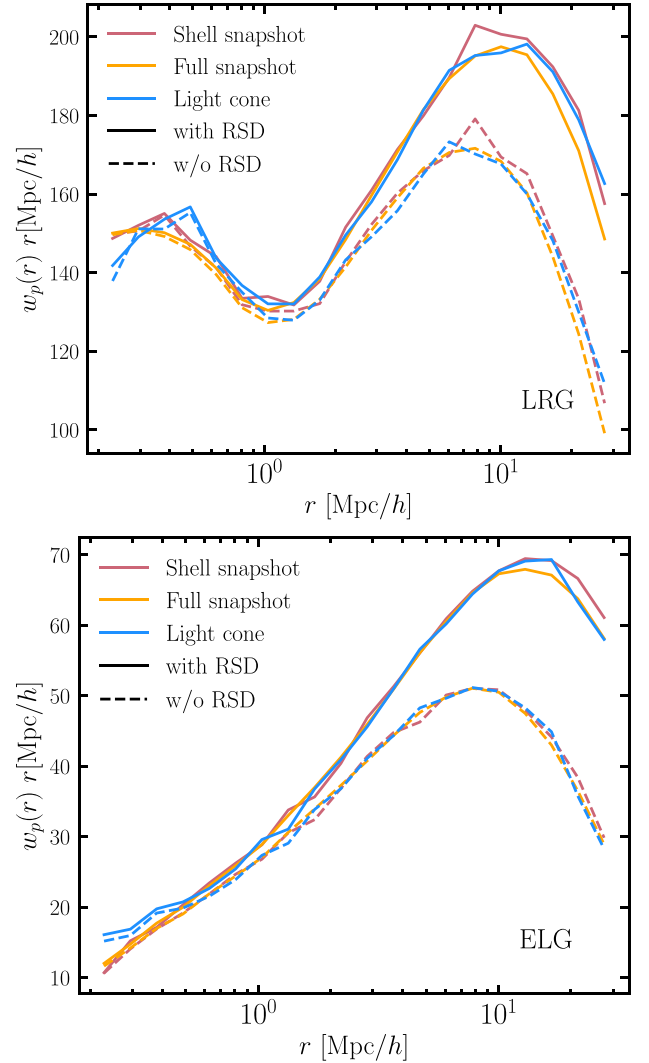

Figure 7. The galaxy projected autocorrelation function computed using the full periodic box (orange), the light-one galaxy catalogue (blue), and an octant shell of the periodic box (red) at the lens redshift, $z_l = 0.8$, integrated out to $\pi_{\max} = 30\,h^{-1}$ Mpc. The top panel displays the LRG result, whereas the bottom one displays the ELG one (defined in Section 2.4). We also show the effect of RSD on the clustering (solid and dashed lines). To isolate redshift evolution effects in the light-one catalogues, we select a thin slice around z_l of thickness $\Delta z = 0.04$. We find that the agreement between all curves is excellent, validating our catalogue construction pipeline. Results are shown for `AbacusSummit_base_c000_ph002`.

where π indicates the distance along the line-of-sight, $DD(r,\pi)$, $DR(r,\pi)$, and $RR(r,\pi)$ are the normalized data–data, data–random, and random–random pair counts as a function of pair distance in the perpendicular (r) and parallel (π) directions. The summation over π indicates that we integrate pairs with line-of-sight separations out to $\pi_{\max} = 30\,h^{-1}$ Mpc.

In Fig. 7, we show the projected autocorrelation function computed using the full periodic box, the light-cone galaxy catalogue, and an octant shell of the periodic box (which has the same thickness and geometry as the light-cone catalogue) at the lens redshift, $z_l = 0.8$. We choose this redshift, as it is the only redshift that the two tracers share in the GQC mocks (Yuan & DESI Collaboration 2023). The top panel shows the result for the LRG galaxy catalogue, whereas the bottom one does so for the ELG one (see definitions of the two
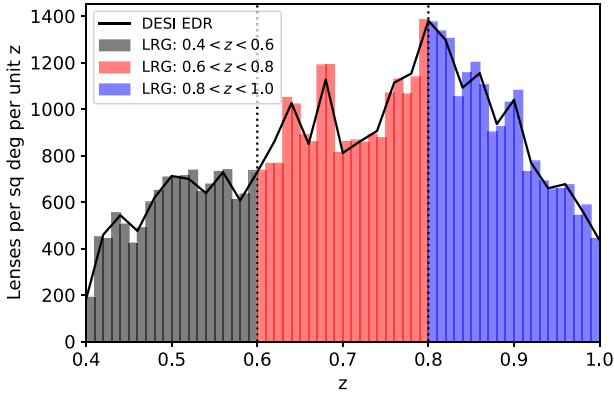
Figure 8. The angular density of selected DESI LRG galaxies in the ABACUSSUMMIT mock as a function of redshift, displayed as a histogram in $\Delta z = 0.01$ bins. Targets from the LRG samples are divided into three lens redshift samples (0.4–0.6, 0.6–0.8, 0.8–1.0) as indicated by the histogram colours and vertical dashed lines. The solid line indicates the measurement from the DESI Early Data Release.

populations in Section 2.4). We also test the effect of switching on and off redshift space distortions (RSD) effects (solid and dashed lines, respectively) to make sure those are properly accounted for. To isolate redshift evolution effects in the light-cone catalogues, we select a thin slice around z_l of thickness $\Delta z = 0.04$. We adopt the corresponding comoving radial distance cut when defining the shell snapshot to ensure that the volume (and thus sample variance effects) are similar in both. We find that the agreement between all three samples for both galaxy populations is excellent, which validates both the light-cone catalogue construction as well as the evolving HOD pipeline used to define the HOD parameters used in each light-cone epoch (see Sections 2.3 and 2.4).

5 OBSERVATIONS PIPELINE

5.1 Mock DESI samples

We downsampled the galaxy catalogues produced via the procedures outlined in Section 2.4 to match the expected redshift distributions $N(z)$ of each respective survey. In the case of DESI, we use the Early Data Release (EDR) catalogues to calculate the comoving number density as a function of redshift (DESI Collaboration 2023). The target $N(z)$ distribution of the DESI EDR is shown in Fig. 8, along with the redshift distribution of our downsampled samples. We produced catalogues in three redshift bins $0.4 < z < 0.6$, $0.6 < z < 0.8$, and $0.8 < z < 1.0$, which are designed to represent a future tomographic analysis of the DESI LRG sample.

We also created random catalogues matching the distribution of each mock DESI samples, for use in the correlation function measurements described in Section 5.3. We drew the angular coordinates randomly from the light-cone mask at reach redshift, and sampled random redshifts from the ensemble of data redshifts.

5.2 Mock source samples

We assigned observational properties to our simulated lensing source populations, statistically drawn from the characteristics of the three weak lensing survey catalogues. These properties include: photometric redshift, shape noise, shear calibration correction, and source weight for weak lensing analyses. In the following subsections, we

detail our implementations for each weak lensing survey, and validate that we successfully replicate the ensemble statistics of each survey.

For convenience, we created simulated shape catalogues with areas roughly matching the overlap of each weak lensing survey with DESI Y1 observations. We implemented this partition by dividing the complete simulated source catalogues into angular pixels of area ≈ 53.7 deg^2 using a HEALPIX pixelization with resolution parameter $n_{\rm side} = 8$. We then grouped these pixels into contiguous regions, using (9, 16, 3) pixels to build each (KiDS, DES, HSC) mock shape catalogue. We ensured that all contributing pixels possessed complete data along the light-cone to $z = 2$, such that each individual ABACUSSUMMIT mock can be used to produce (4, 2, 12) catalogues representing the overlap of DESI Y1 and (KiDS, DES, HSC).

5.2.1 KiDS

We based our KiDS source mocks on the KiDS-1000 'gold sample' data set (Giblin et al. 2021), which consists of 21 million galaxies with an effective number density $n_{\rm eff} = 6.2$ gal/arcmin^2. The shape catalogue is divided for analysis into five tomographic bins with edges $z_B = [0.1, 0.3, 0.5, 0.7, 0.9, 1.2]$, based on point photometric redshift estimates z_B of the BPZ method. Ellipticity measurements and weights for each source were provided by a self-calibrating version of LENSFIT (Fenech Conti et al. 2017).

We first subsampled the ABACUSSUMMIT source halo catalogues in a series of narrow redshift slices, using a minimum halo mass to match the source density of the KiDS-1000 sample in those slices calibrated by Hildebrandt et al. (2021). In order to re-create the division into tomographic source bins, we then statistically assigned photometric redshifts z_p to each mock source from a scattering probability distribution $P(z_p|z_s)$ conditional on the 'spectroscopic' or true simulation redshift z_s. We built this probability map using the redshift calibration reference sample built by the KiDS collaboration (Hildebrandt et al. 2021), which is re-weighted using a self-organizing map to closely resemble the distribution of KiDS-1000 sources.[3]

Next, we distorted the noise-free shear components from the simulated lensing fields to account for multiplicative shear calibration factors present in the shape catalogues, and statistical shape noise error. Following table 1 of Giblin et al. (2021), we assigned shear calibration corrections $m = [-0.009, -0.011, -0.015, 0.002, 0.007]$ and ellipticity dispersions per component $\sigma_e = [0.270, 0.258, 0.273, 0.254, 0.270]$ in the five tomographic bins. We first applied the shear calibration correction by multiplying the noise-free shear components in each bin by $(1 + m)$. We then introduced shape noise to the source catalogues by determining the complex noisy shear $e = (\gamma + n)/(1 + n\gamma^*)$ (Seitz & Schneider 1997), where the components of observed shear (e_1, e_2) are found as $e = e_1 + ie_2$, the noise-free shear $\gamma = \gamma_1 + i\gamma_2$, and the noise $n = n_1 + in_2$. The noise components (n_1, n_2) are drawn from Gaussian distributions with standard deviation σ_e. Finally, we assigned weights to each lensing source by randomly subsampling from the LENSFIT weights of the survey data set within each tomographic bin.

This procedure resulted in a suite of KiDS source mocks with ensemble properties representing those of the real catalogues in each tomographic bin: redshift distribution, source weights, multiplicative shear calibration factors, and shape noise. We repeated this procedure

---

[3]We are grateful to Hendrik Hildebrandt for sharing this catalogue for the purpose of constructing these mocks.

to create DES and HSC mocks, emphasizing some aspects specific to these surveys in the following subsections.

5.2.2 DES

We based our DES source mocks on the DES Year 3 (DES-Y3) weak lensing shape catalogue (Gatti et al. 2021), which was derived using the METACALIBRATION pipeline, and consists of 100.2 million galaxies with an effective number density $n_{\mathrm{eff}} = 5.6$ gal/arcmin^2. Galaxies in the DES-Y3 data set are clustered by a self-organizing map into different 'phenotypes', which are used to construct four tomographic source bins with edges $z_p = [0.0, 0.36, 0.63, 0.87, 2.0]$ (Myles et al. 2021). In the METACALIBRATION framework, all sources are assigned a shear response matrix **R** (Gatti et al. 2021), which we approximate for our purposes by the leading-order diagonal elements R_{11} and R_{22} such that the shear calibration correction is a scalar quantity $(R_{11} + R_{22})/2$. The DES-Y3 framework also allows for a residual multiplicative bias with best values $m = [-0.006, -0.020, -0.024, -0.037]$ in the four tomographic bins (Amon et al. 2022).

After subsampling the mock halo catalogues as a function of true redshift z_s to match the DES-Y3 source redshift distribution, we statistically assigned a tomographic bin $b = (1, 2, 3, 4)$ to each mock source using a scattering probability distribution $P(b|z_s)$ constructed from the source density and calibrated redshift distribution in each tomographic bin. We randomly assigned values of R_{11}, R_{22} and weight to each mock source, drawn from the real DES-Y3 data catalogue in each tomographic bin, and applied the shear calibration correction by multiplying the noise-free shear components in each bin by $(1 + m) \times (R_{11} + R_{22})/2$. Finally, we applied shape noise to the distorted noise-free shear components using the formulation described in Section 5.2.1, where we take $\sigma_e = [0.201, 0.204, 0.195, 0.203]$ in the four tomographic bins. These noise values differ from those quoted in table 1 of Amon et al. (2022), because we are applying them to ellipticities which have already been distorted by the shear responsivity. The overall shape noise, including calibration factors, matches the noise properties of DES-Y3.

This procedure resulted in a suite of DES-Y3 source mocks with assigned tomographic bins, distorted and noisy ellipticities, shear calibration factors (R_{11}, R_{22}), and lensing weights.

5.2.3 HSC

We based our HSC mocks on the HSC-Y1 weak lensing shape catalogue (Mandelbaum et al. 2018), which comprises 9 million galaxies with an effective number density $n_{\mathrm{eff}} = 17.6$ gal/arcmin^2. Sources are assigned into four tomographic bins using point estimates from the EPHOR photo-z code (Hikage et al. 2019). The shear estimators in HSC use a responsivity factor $2R$ (see equation 3 in Mandelbaum et al. 2018), where $R = 1 - e_{\mathrm{rms}}^2$ and e_{rms} is the rms intrinsic distortion per component, along with a residual multiplicative bias m. Finally, sources are assigned an inverse-variance shape weight w based on a quadrature sum of shape noise and measurement error (Mandelbaum et al. 2018).

As described in Section 5.2.1, we statistically assigned photometric redshifts to each mock source from a scattering probability distribution calibrated by the HSC redshift calibration sample (Hikage et al. 2019). We randomly assigned values of shape weight w, e_{rms}, and m to each mock source, drawn from the real HSC data catalogue in each tomographic bin, and applied the shear calibration correction by multiplying the noise-free shear components in each bin by $(1 + m) \times 2 \left(1 - e_{\mathrm{rms}}^2\right)$. Finally, we applied the noise to the

distorted noise-free shear components, where we deduced the noise to be applied to each source as $\sigma_e = 1/\sqrt{w}$ (which combines both shape noise and measurement error).

This procedure resulted in a suite of HSC source mocks with assigned tomographic bins, distorted and noisy ellipticities, shear calibration factors (e_{rms}, m), and lensing weights.

5.2.4 Summary statistics

Before testing the correlation properties of these source mocks, we first validated that their ensemble statistical properties in each tomographic bin matched each weak lensing survey. Fig. 9 displays the spectroscopic redshift distributions of each separate tomographic sample of the KiDS, DES, and HSC source mocks. The distributions are compared to those defined for the data samples by each survey collaboration, demonstrating that the source mocks are representative of the data. The only significant discrepancy is found at the lowest redshifts, where there is a small deficit of mock sources because the mass resolution of the mocks is insufficient to match the number density of the deepest weak lensing catalogues at low redshift. However, low-redshift sources have little constraining power for weak lensing, such that this deficit is unimportant. The 'spikes' in the redshift distribution of Fig. 9 correspond to sample variance fluctuations in the spectroscopic reference sets used by each lensing collaboration.

Fig. 10 compares some ensemble properties of each separate tomographic sample of the KiDS, DES, and HSC ABACUSSUMMIT source mocks, and the corresponding survey data catalogues. The ensemble properties considered are the effective source number density, effective shape noise, average source weight, and standard deviation of the source weight. The effective number density is defined in terms of the source weights w_i for each galaxy, following Heymans et al. (2012), by

$$n_{\mathrm{eff}} = \frac{1}{A} \frac{\left(\sum_i w_i\right)^2}{\sum_i w_i^2}, \tag{34}$$

where A is the area covered by the catalogue, and the effective shape variance by

$$\sigma_e^2 = \frac{1}{2} \left[\frac{\sum_i w_i^2 e_{i,1}^2}{\sum_i w_i^2} + \frac{\sum_i w_i^2 e_{i,2}^2}{\sum_i w_i^2} \right]. \tag{35}$$

Fig. 10 shows good agreement between the properties of the mock and data catalogues.

5.3 Correlation function tests of the mock samples

We validated the ABACUSSUMMIT weak lensing and DESI mock catalogues by comparing their measured two-point correlation functions to theoretical predictions. We note that full cosmological parameter fits with analytical covariance are beyond the scope of this study, and will be presented by future work. The scope of this section is to simply present the correlation function measurements, and check for any significant discrepancies with theoretical predictions that would indicate serious failures in mock construction.

First, we measured the cosmic shear correlation functions $\xi_{\pm}(\theta)$ of the different source catalogues in tomographic bins, using the TREECORR package (Jarvis 2015). We performed measurements using the same angular separation binning adopted by each weak lensing collaboration when presenting their cosmic shear results. Fig. 11 displays the shear correlation function measurements for the DES mocks in four tomographic bins (results for the KiDS and
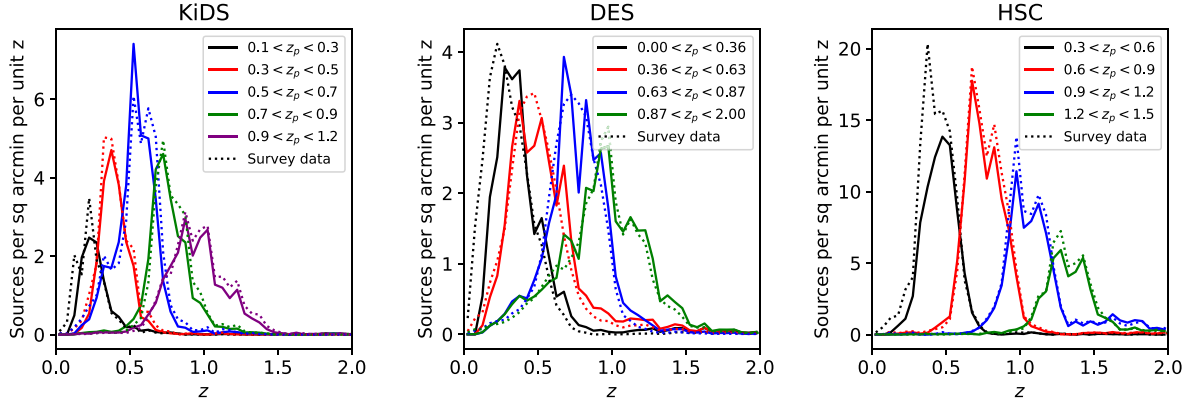
Figure 9. The angular density of mock source galaxies in the KiDS (left-hand panel), DES (middle panel), and HSC (right-hand panel) ABACUSSUMMIT mocks as a function of spectroscopic redshift. Separate redshift distributions are plotted for each source tomographic sample, and the measurements from the mocks (solid lines) and compared to the redshift probability distributions defined for the data samples by each survey collaboration (dotted lines).
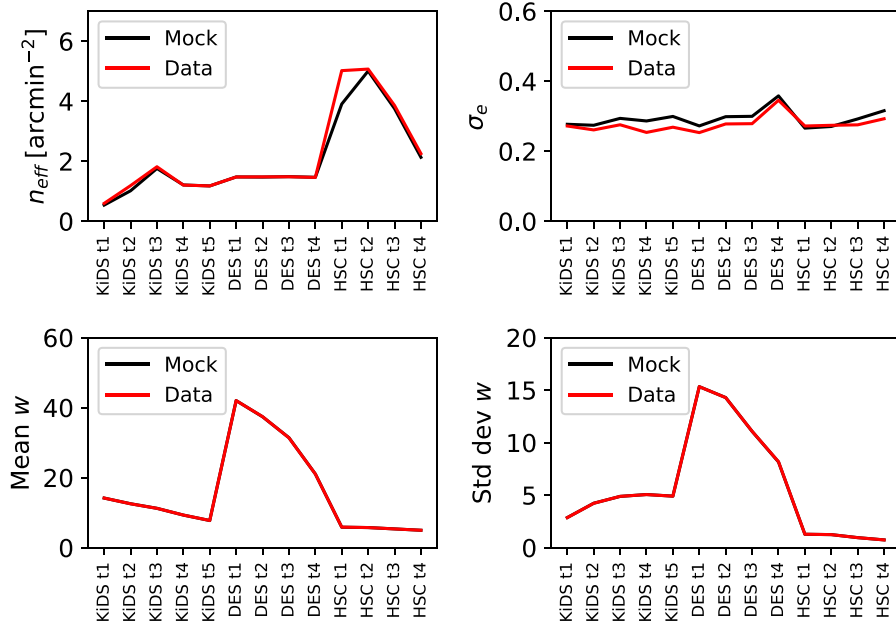

Figure 10. Comparison of some ensemble properties of the KiDS, DES, and HSC ABACUSSUMMIT source mocks, and the corresponding data catalogues of those surveys. Results are displayed for each source tomographic sample (5 for KiDS, 4 for DES, and 4 for HSC). The ensemble properties considered are the effective source number density n_{eff} (top left panel), the effective shape noise σ_e (top right panel), the mean source weight (bottom left panel), and the standard deviation of the source weight across the sample (bottom right panel).

HSC mocks have a similar presentation, and we do not show them). We plot the mean and standard deviation of the measurements for the different DES regions (which have areas representative of the overlap of the DES Y3 and DESI Y1 data sets), compared to the fiducial cosmological models in each case, computed from the source redshift distributions and ABACUSSUMMIT matter power spectra. The measured correlation functions are corrected for the applied shear calibration factors included in the mock outputs. We find that the fiducial models provide a good description of these measurements.

Next, we measure the average tangential shear (galaxy–galaxy lensing signal) $\gamma_t(\theta)$ between the mock source catalogues and the lens samples of the DESI ABACUSSUMMIT mocks, again using TREECORR and adopting the same angular separation bins as before. Fig. 12

displays these measurements between the four tomographic source samples of the DES mocks, around the three lens samples of the DESI mocks (results for the KiDS and HSC mocks have a similar appearance). We plot the mean and standard deviation of the measurements for the different DES regions, compared to the fiducial cosmological models in each case, assuming a representative linear bias factor $b = 2$. We again note that the fiducial models provide a good description of these measurements, except at small scales, where the linear bias formulation is inaccurate.

Finally, we measure the correlation function multipoles of the DESI ABACUSSUMMIT mocks in the three redshift bins (0.4–0.6, 0.6–0.8, 0.8–1.0), using the CORRFUNC package (Sinha & Garrison 2020). We perform monopole and quadrupole measurements in 20 linearly
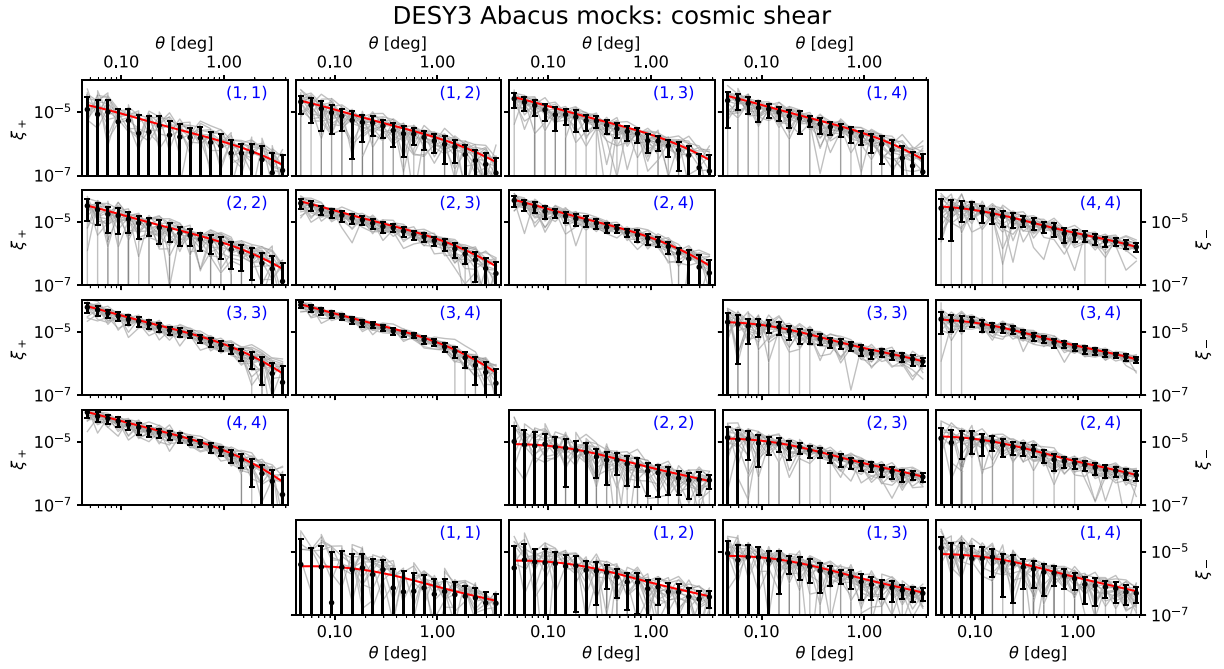
DESY3 Abacus mocks: cosmic shear

Figure 11. The shear correlation functions (ξ_+, ξ_-) between the four tomographic source samples of the DES ABACUSSUMMIT mocks, as a function of angular separation θ in degrees. The different panels display measurements for different combinations of tomographic samples, as indicated by the identifiers in the top right corner of each panel. We plot the mean and standard deviation of the measurements across the ABACUSSUMMIT DES regions, where the light grey lines indicate measurements for a selection of individual regions. The solid lines show the fiducial cosmological models for (ξ_+, ξ_-).

DESY3 Abacus mocks: galaxy-galaxy lensing
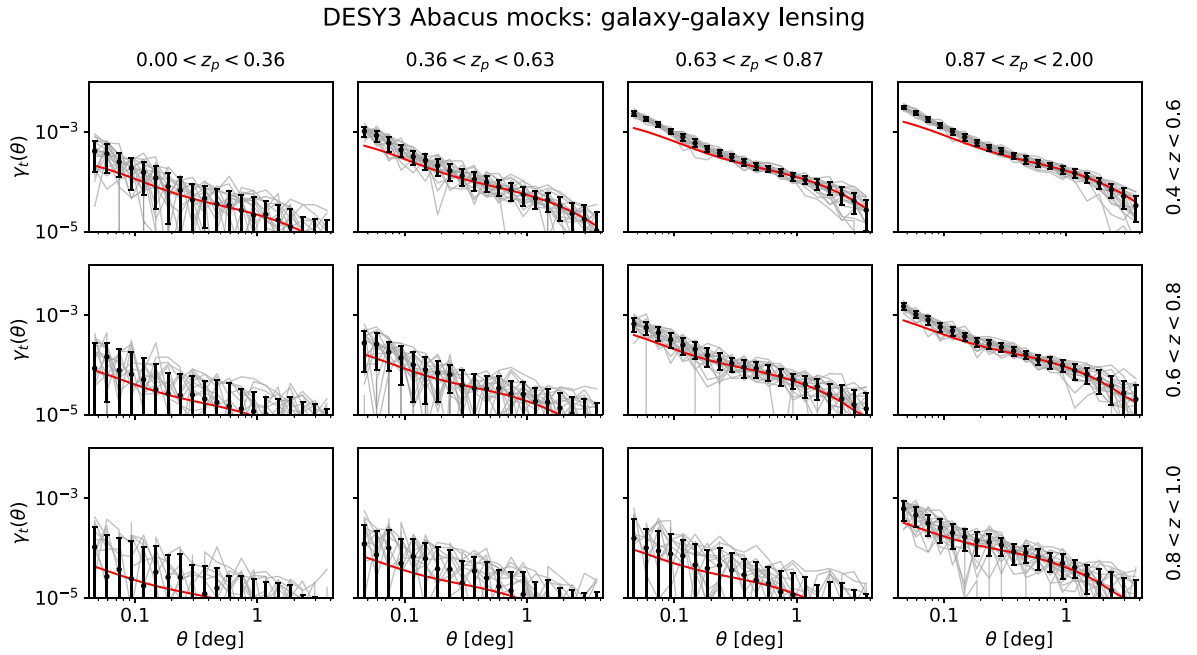
Figure 12. The average tangential shear γ_t of the four tomographic source samples of the DES ABACUSSUMMIT mocks, around the three lens samples of the DESI ABACUSSUMMIT mocks, as a function of angular separation θ in degrees. The different panels display measurements for different combinations of source and lens samples, as indicated by the captions above and to the right of each panel. We plot the mean and standard deviation of the measurements across the DES regions, where the light grey lines indicate measurements for a selection of individual regions. The solid lines show the fiducial cosmological models for γ_t, assuming a representative linear galaxy bias factor.

DESI Abacus mocks: correlation function multipoles
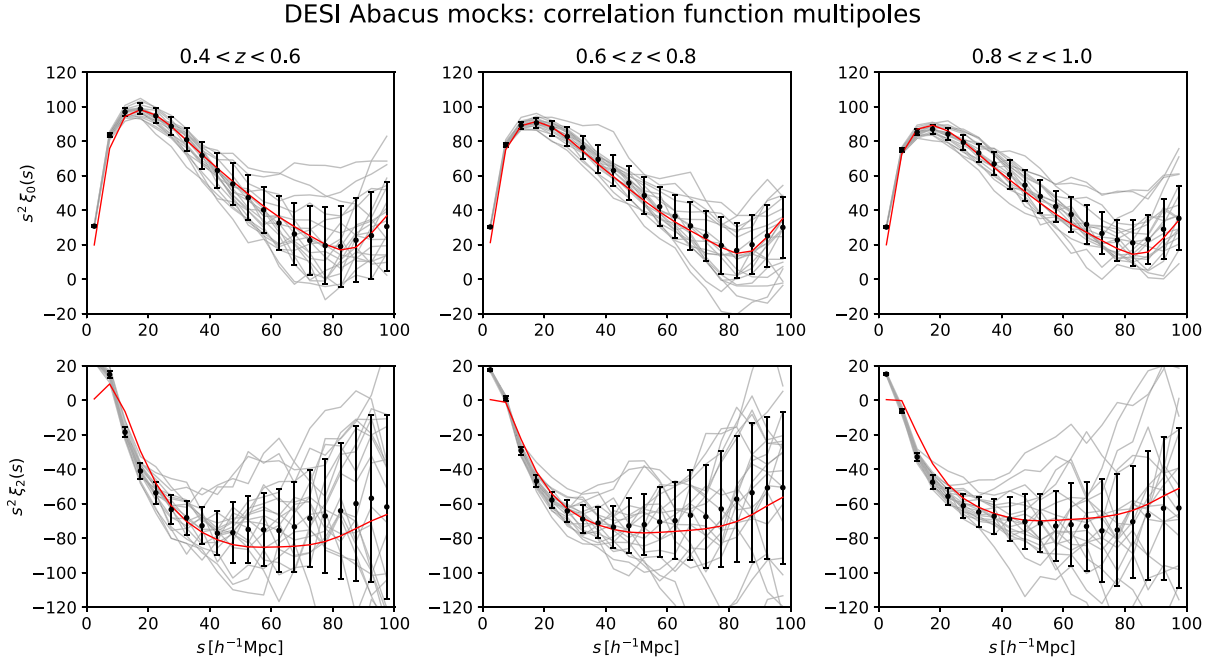
Figure 13. The monopole and quadrupole correlation function ξ_0 and ξ_2 of the three lens samples of the DESI ABACUSSUMMIT mocks, as a function of spatial separation s in units of h^{-1} Mpc. We plot the mean and standard deviation of the measurements across the DES regions, where the light grey lines indicate measurements for a selection of individual regions. The solid lines show the fiducial cosmological models, assuming a representative linear galaxy bias factor and RSD streaming model.

spaced separation bins between 0 and $100\,h^{-1}$ Mpc. Fig. 13 displays these correlation function multipole measurements for the DESI mocks in the DES regions. We plot the mean and standard deviation of the measurements for the different regions, compared to the fiducial cosmological models in each case, assuming a representative linear bias factor $b = 2$ and RSD streaming model with small-scale velocity dispersion $\sigma_v = 300$ km s^{-1}. The fiducial models provide a good description of the signals, except at small scales where the linear RSD prescription breaks down.

6 SUMMARY

In this paper, we present high-resolution curved-sky weak lensing maps, generated using the Born approximation and the *N*-body simulation suite ABACUSSUMMIT, as well as accompanying weak lensing mock catalogues, which are tuned via fits to DESI small-scale clustering measurements of LRGs and ELGs. We make these products publicly available at app.globus.org. The purpose of these products is to aid the joint analysis between galaxy surveys such as DESI and weak lensing surveys such as HSC, DES, and KiDS.

In Section 3, we provide a detailed description of our procedure for generating the weak lensing maps, which follows the 'Onion Universe' approach (Fosalba et al. 2015), as well as various validation plots. The available maps consist of the cosmic shear, deflection angle and convergence fields at source redshifts ranging from $z = 0.15$ to 2.45 with $\Delta z = 0.05$ as well as CMB convergence maps ($z \approx 1089.3$) for each of the 25 base-resolution simulations ($L_{\text{box}} = 2000\,h^{-1}$ Mpc and $N_{\text{part}} = 6912^3$) as well as for the two huge simulations ($L_{\text{box}} = 7500\,h^{-1}$ Mpc and $N_{\text{part}} = 8640^3$) at the fiducial AbacusSummit cosmology (*Planck* 2018). The pixel resolution of each map is 0.21 arcmin, corresponding to a HEALPIX

N_{side} of 16 384. The sky coverage of the base simulations is an octant until $z \approx 0.8$ (decreasing to about 1800 deg^2 at $z \approx 2.4$), whereas the huge simulations offer full-sky coverage until $z \approx 2.2$.

As validation of the source maps and catalogues, we study the angular power spectrum of the convergence field, $C_\ell^{\kappa\kappa}$, shown in Fig. 3, and the shear autocorrelation, $\xi_\pm(\theta)$, shown in Fig. 4. We find that the base-resolution simulations show a remarkable agreement with the theoretical prediction for $C_\ell^{\kappa\kappa}$ from PYCCL, which in turn employs the HALOFIT matter power spectrum. The huge-resolution result displays a larger deviation from PYCCL (though is in great agreement with Cosmic Emu), which we attribute to resolution effects and explore further in Appendix B. The shear–shear angular correlation function from ABACUSSUMMIT also shows excellent agreement with theory in most regimes, but suffers from boundary effects in the $\xi_+(\theta)$ measurement for $\theta > 100$ arcmin. We note, however, that the errors are still within the noise of the weak lensing surveys of interest to this work, and the deficit is not visible when mimicking these surveys near $\theta \sim 200$ arcmin (see Fig. 11). These are investigated in detail in Appendix A. We comment that the cut-off of ξ_- relative to PYCCL at $\theta < 1$ arcmin is due to resolution effects (i.e. the pixel size of 0.21 arcmin), which are pushed to larger scales for ξ_- than ξ_+.

In Section 4, we describe our process for assigning lensing properties ($\gamma_{1,2}$) to our source population, which covers the redshift range between $z = 0.15$ and 2, as well as our implementation of magnification bias for the lens population of LRGs and ELGs, which covers the redshift range between $z = 0.3$ and 1.4. To enable the application of magnification bias to our HOD catalogues, we record the lensed positions and appropriate weights accounting for flux magnification for each lens galaxy. We then validate the mock creation procedure by comparing to PYCCL, which adopts a simple

linear bias approximation. As expected, we find reasonable agreement on large scales between the galaxy–galaxy lensing observables, $C_\ell^{\kappa g}$ and $\gamma_t(\theta)$, but on small scales, the linear bias model shows substantial deviations, overpredicting the clustering of ELGs and underpredicting that of the LRGs (see Figs 5 and 6). Furthermore, we generate random catalogues for the lens population of galaxies, which can be used to measure the galaxy autocorrelation. In Fig. 7, we show the projected galaxy clustering, $w_p(r)$, with and without redshift space distortions for both LRGs and ELGs, and compare it with two samples generated using the periodic box, finding exquisite agreement.

In Section 5, we subsample the ABACUSSUMMIT halo mocks to match the redshift distributions of the DESI Early Data Release, and the ensemble properties of the KiDS, DES, and HSC weak lensing data sets. We perform a statistical assignment of photometric redshifts to partition the data into tomographic bins matching those chosen by the lensing survey collaborations, and we also apply shear calibration corrections and shape noise in the framework of these surveys. Finally, we verify that the cosmic shear correlation functions, galaxy–galaxy lensing signal, and clustering multipole correlation functions of these catalogues agree with those predicted in the fiducial cosmology.

An immediate application of our products, planned for the near-term, is to extensively test the pipelines developed for analysing redshift and weak lensing surveys, and ensure they are capable of correctly recovering the underlying cosmology and robust to various systematic and observational effects. A longer term goal is to construct an emulator and use it to constrain astrophysical (e.g. galaxy–halo connection) and cosmological parameters from combinations of the latest galaxy and weak lensing data sets. We are also planning to implement beyond-Born approximation corrections and baryonic effects, which would allow us to more reliably model ∼0.1 arcmin scales.

ACKNOWLEDGEMENTS

DATA AVAILABILITY

The data and accompanying scripts are publicly available and stored as a NERSC shared endpoint, 'AbacusSummit Weak Lensing', at https://app.globus.org/file-manager?origin_id=3dd6566c-eed2-11ed-ba43-09d6a6f08166&path=~per~cent2F. Data points for the figures are available at https://doi.org/10.5281/zenodo.7926269.

REFERENCES

Abbott T. M. C. et al., 2018, Phys. Rev. D, 98, 043526
Aihara H. et al., 2018, PASJ, 70, S4
Alam S., Peacock J. A., Kraljic K., Ross A. J., Comparat J., 2020, MNRAS, 497, 581
Amendola L. et al., 2013, Living Rev. Relativ., 16, 6
Amon A. et al., 2022, Phys. Rev. D, 105, 023514
Bartelmann M., Schneider P., 2001, Phys. Rep., 340, 291
Baugh C. M., 1996, MNRAS, 280, 267
Baugh C. M., 2006, Rep. Prog. Phys., 69, 3101
Becker M. R., 2013, MNRAS, 435, 115
Benítez N., Martínez-González E., 1997, ApJ, 477, 27
Benson A. J., 2012, New Astron., 17, 175
Berlind A. A., Weinberg D. H., 2002, ApJ, 575, 587
Bernardeau F., Colombi S., Gaztañaga E., Scoccimarro R., 2002, Phys. Rep., 367, 1
Blandford R. D., Saust A. B., Brainerd T. G., Villumsen J. V., 1991, MNRAS, 251, 600
Blumenthal G. R., Faber S. M., Primack J. R., Rees M. J., 1984, Nature, 311, 517
Bose S., Eisenstein D. J., Hadzhiyska B., Garrison L. H., Yuan S., 2022, MNRAS, 512, 837
Brainerd T. G., Blandford R. D., Smail I., 1996, ApJ, 466, 623
Cacciato M., van den Bosch F. C., More S., Li R., Mo H. J., Yang X., 2009, MNRAS, 394, 929
Chisari N. E. et al., 2019, ApJS, 242, 2
Choi A., Tyson J. A., Morrison C. B., Jee M. J., Schmidt S. J., Margoniner V. E., Wittman D. M., 2012, ApJ, 759, 101
Clampitt J. et al., 2017, MNRAS, 465, 4204
Cole S. et al., 2005, MNRAS, 362, 505
Collins C. A., Nichol R. C., Lumsden S. L., 1992, MNRAS, 254, 295
Conroy C., Wechsler R. H., Kravtsov A. V., 2007, ApJ, 668, 826
Dark Energy Survey Collaboration, 2016, MNRAS, 460, 1270
Das S., Bode P., 2008, ApJ, 682, 1
DeRose J. et al., 2019, preprint (arXiv:1901.02401)
DESI Collaboration, 2016a, preprint (arXiv:1611.00036)
DESI Collaboration, 2016b, preprint (arXiv:1611.00037)
DESI Collaboration, 2022, AJ, 164, 207
DESI Collaboration, 2023, preprint (arXiv:2306.06308)
Eisenstein D. J., Zaldarriaga M., 2001, ApJ, 546, 2
Fenech Conti I., Herbonnet R., Hoekstra H., Merten J., Miller L., Viola M., 2017, MNRAS, 467, 1627
Ferlito F. et al., 2023, MNRAS, 524, 5591
Fischer P. et al., 2000, AJ, 120, 1198
Flaugher B. et al., 2015, AJ, 150, 150
Fosalba P., Gaztañaga E., Castander F. J., Manera M., 2008, MNRAS, 391, 435
Fosalba P., Gaztañaga E., Castander F. J., Crocce M., 2015, MNRAS, 447, 1319
Garrison L. H., Eisenstein D. J., Ferrer D., Tinker J. L., Pinto P. A., Weinberg D. H., 2018, ApJS, 236, 43
Garrison L. H., Eisenstein D. J., Pinto P. A., 2019, MNRAS, 485, 3370
Garrison L., Eisenstein D., Ferrer D., Maksimova N., Pinto P., 2021, MNRAS, 508, 575
Gatti M. et al., 2021, MNRAS, 504, 4312
Gaztañaga E., 2003, ApJ, 589, 82
Gaztanaga E., Bernardeau F., 1998, A&A, 331, 829
Giblin B. et al., 2021, A&A, 645, A105

Gonzalez-Perez V. et al., 2020, MNRAS, 498, 1852
Groth E. J., Peebles P. J. E., 1977, ApJ, 217, 385
Hadzhiyska B., Bose S., Eisenstein D., Hernquist L., Spergel D. N., 2020, MNRAS, 493, 5506
Hadzhiyska B., Bose S., Eisenstein D., Hernquist L., 2021a, MNRAS, 501, 1603
Hadzhiyska B., Tacchella S., Bose S., Eisenstein D. J., 2021b, MNRAS, 502, 3599
Hadzhiyska B., Garrison L. H., Eisenstein D., Bose S., 2022, MNRAS, 509, 2194
Hadzhiyska B. et al., 2023a, MNRAS, 524, 2507
Hadzhiyska B. et al., 2023b, MNRAS, 524, 2524
Hamana T., Colombi S. T., Thion A., Devriendt J. E. G. T., Mellier Y., Bernardeau F., 2002, MNRAS, 330, 365
Hamilton A. J. S., Tegmark M., 2002, MNRAS, 330, 506
Harnois-Déraps J. et al., 2018, MNRAS, 481, 1337
Heitmann K. et al., 2016, ApJ, 820, 108
Heymans C. et al., 2012, MNRAS, 427, 146
Heymans C. et al., 2021, A&A, 646, A140
Hikage C. et al., 2019, PASJ, 71, 43
Hilbert S., Hartlap J., White S. D. M., Schneider P., 2009, A&A, 499, 31
Hildebrandt H. et al., 2021, A&A, 647, A124
Hu W., 2000, Phys. Rev. D, 62, 043007
Hu W., Jain B., 2004, Phys. Rev. D, 70, 043009
Huterer D., Knox L., Nichol R. C., 2001, ApJ, 555, 547
Jain B., Seljak U., White S., 2000, ApJ, 530, 547
Jain B., Scranton R., Sheth R. K., 2003, MNRAS, 345, 62
Jarvis M., 2015, Astrophysics Source Code Library, record ascl:1508.007
Jiménez E., Contreras S., Padilla N., Zehavi I., Baugh C. M., Gonzalez-Perez V., 2019, MNRAS, 490, 3532
Johnston D. E. et al., 2007, preprint (arXiv:0709.1159)
Kacprzak T., Fluri J., Schneider A., Refregier A., Stadel J., 2023, J. Cosmol. Astropart. Phys., 2023, 050
Kaiser N., 1992, ApJ, 388, 272
Korytov D. et al., 2019, ApJS, 245, 26
Kravtsov A. V., Berlind A. A., Wechsler R. H., Klypin A. A., Gottlöber S., Allgood B., Primack J. R., 2004, ApJ, 609, 35
Kuijken K. et al., 2015, MNRAS, 454, 3500
Kwan J. et al., 2017, MNRAS, 464, 4045
Leauthaud A. et al., 2012, ApJ, 744, 159
Leauthaud A. et al., 2017, MNRAS, 467, 3024
Lemos P., Challinor A., Efstathiou G., 2017, J. Cosmol. Astropart. Phys., 2017, 014
Levi M. et al., 2013, preprint (arXiv:1308.0847)
Levi M. et al., 2019, BAAS, 51, 57
Lewis A., 2005, Phys. Rev. D, 71, 083008
Limber D. N., 1953, ApJ, 117, 134
LoVerde M., Afshordi N., 2008, Phys. Rev. D, 78, 123506
LSST Dark Energy Science Collaboration, 2012, preprint (arXiv:1211.0310)
Maddox S. J., Sutherland W. J., Efstathiou G., Loveday J., 1990, MNRAS, 243, 692
Maddox S. J., Efstathiou G., Sutherland W. J., 1996, MNRAS, 283, 1227
Maksimova N., Garrison L., Eisenstein D., Hadzhiyska B., Bose S., Satterthwaite T., 2021a, MNRAS, 508, 4018
Maksimova N. A., Garrison L. H., Eisenstein D. J., Hadzhiyska B., Bose S., Satterthwaite T. P., 2021b, MNRAS, 508, 4017
Maleubre S., Eisenstein D., Garrison L. H., Joyce M., 2022, MNRAS, 512, 1829
Mandelbaum R., 2018, ARA&A, 56, 393
Mandelbaum R., Seljak U., Kauffmann G., Hirata C. M., Brinkmann J., 2006, MNRAS, 368, 715
Mandelbaum R., Slosar A., Baldauf T., Seljak U., Hirata C. M., Nakajima R., Reyes R., Smith R. E., 2013, MNRAS, 432, 1544
Mandelbaum R. et al., 2018, PASJ, 70, S25
Moessner R., Jain B., 1998, MNRAS, 294, L18
Myers A. D., Outram P. J., Shanks T., Boyle B. J., Croom S. M., Loaring N. S., Miller L., Smith R. J., 2005, MNRAS, 359, 741
Myles J. et al., 2021, MNRAS, 505, 4249
Padmanabhan N. et al., 2007, MNRAS, 378, 852
Peacock J. A., Smith R. E., 2000, MNRAS, 318, 1144
Percival W. J. et al., 2001, MNRAS, 327, 1297
Prat J. et al., 2018, Phys. Rev. D, 98, 042005
Saunders W. et al., 2000, MNRAS, 317, 55
Schneider P., van Waerbeke L., Kilbinger M., Mellier Y., 2002, A&A, 396, 1
Scoccimarro R., Sheth R. K., Hui L., Jain B., 2001, ApJ, 546, 20
Scranton R. et al., 2005, ApJ, 633, 589
Seitz C., Schneider P., 1997, A&A, 318, 687
Seljak U., 2000, MNRAS, 318, 203
Silber J. H. et al., 2023, AJ, 165, 9
Sinha M., Garrison L. H., 2020, MNRAS, 491, 3022
Somerville R. S., Hopkins P. F., Cox T. J., Robertson B. E., Hernquist L., 2008, MNRAS, 391, 481
Szapudi I., Gaztanaga E., 1998, MNRAS, 300, 493
Takahashi R., Sato M., Nishimichi T., Taruya A., Oguri M., 2012, ApJ, 761, 152
Takahashi R., Hamana T., Shirasaki M., Namikawa T., Nishimichi T., Osato K., Shiroyama K., 2017, ApJ, 850, 24
Tegmark M. et al., 2006, Phys. Rev. D, 74, 123507
Teyssier R. et al., 2009, A&A, 497, 335
Vale A., Ostriker J. P., 2004, MNRAS, 353, 189
Vale C., White M., 2003, ApJ, 592, 699
Velander M. et al., 2014, MNRAS, 437, 2111
Wambsganss J., Cen R., Ostriker J. P., 1998, ApJ, 494, 29
White M., Hu W., 2000, ApJ, 537, 1
White M., Vale C., 2004, Astropart. Phys., 22, 19
Xu X., Zehavi I., Contreras S., 2021a, MNRAS, 502, 3242
Xu X., Kumar S., Zehavi I., Contreras S., 2021b, MNRAS, 507, 4879
Yuan S., Garrison L. H., Hadzhiyska B., Bose S., Eisenstein D. J., 2022, MNRAS, 510, 3301
Yuan S. et al., 2023, preprint (arXiv:2306.06314)
Zheng Z. et al., 2005, ApJ, 633, 791

APPENDIX A: TESTING THE PARTIAL SKY SHEAR MAPS

Given the unusual geometric configuration of the ABACUSSUMMIT base light-cones (see Fig. 1), it is important to test the boundary effects on the lensing observables derived through harmonic transforms of the convergence field, i.e. the shear and deflection angle field. To this end, we construct the following simple test using the huge simulations, for which we know the 'truth,' since they cover the entire sky rather than an octant.

Test 1

First, we test the effect of the $\kappa(\hat{n})$ to $\gamma_{1,2}(\hat{n})$ conversion in the event of incomplete sky coverage. In particular, we measure the $\xi_{\pm}(\theta)$ signal for four different scenarios.

(i) Scenario 1: Measuring $\xi_{\pm}$ from the full-sky $\gamma_{1,2}(\hat{n})$ map, which has been obtained from the full-sky $\kappa(\hat{n})$ following equation (17).

(ii) Scenario 2: Measuring $\xi_{\pm}$ from only an octant of the full-sky $\gamma_{1,2}(\hat{n})$ map, obtained from the full-sky $\kappa(\hat{n})$.

(iii) Scenario 3: Measuring $\xi_{\pm}$ from the octant $\gamma_{1,2}(\hat{n})$ map, obtained by converting an octant of $\kappa(\hat{n})$ into $\gamma_{1,2}(\hat{n})$ following equation (17).

(iv) Scenario 4: Measuring $\xi_{\pm}$ from the octant $\gamma_{1,2}(\hat{n})$ map, obtained from an octant of $\kappa(\hat{n})$ multiplied by a mask smoothed at the boundaries with a Gaussian kernel of 2 deg.

In Fig. A2, we show the results of this exercise, finding that the dominant effect causing deviations from theory is cosmic variance, though the partial sky conversion does affect the largest scales. In particular, the curves exhibit minimal differences for $\theta < 100$ arcmin
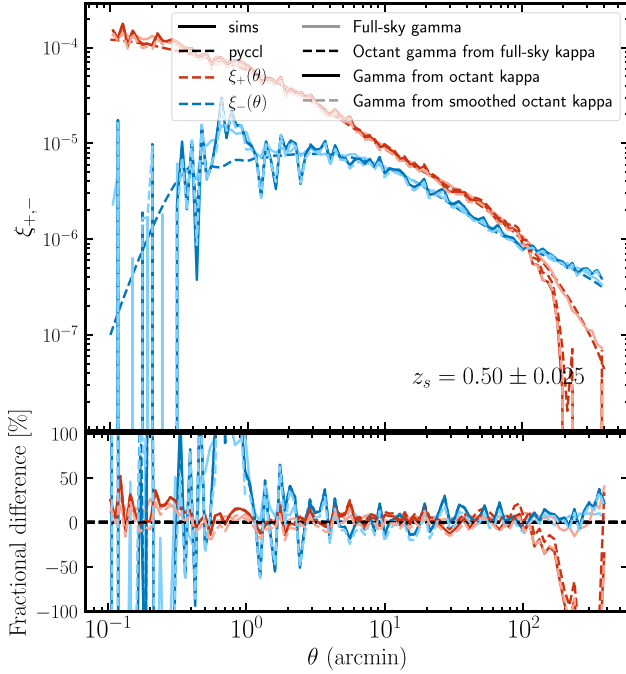
Figure A1. **Test 1**, described in Appendix A, of the shear–shear autocorrelation, $\xi_{\pm}(\theta)$, at source redshift of $z_s = 0.5$, using the AbacusSummit_huge_c000_ph201 simulation. The source catalogue is obtained using downsampled halo and particle catalogues. The full-sky gamma measurements of $\xi_{\pm}(\theta)$ (pale solid lines) agree best with the theoretical prediction, as they do not suffer from boundary effects. We only see noticeable differences with the other curves for $\theta > 100$ arcmin. The maps obtained by converting an octant of $\kappa(\hat{n})$ yield almost identical results regardless of whether a smoothed mask is applied or not (dark solid and pale dashed lines). The γ measurements cut out from the full-sky γ maps (dark dashed lines) exhibit only marginal improvement compared with the other two octant results, suggesting that the main contributor to the noise is sample variance at those scales.

for $\xi_{\pm}(\theta)$, and we only see noticeable deviations past that scale for $\xi_{+}(\theta)$. As expected, the full-sky gamma measurements of $\xi_{\pm}(\theta)$ agree best with the theoretical prediction, as they do not suffer from boundary effects. We further notice that the maps obtained by converting an octant of the $\kappa(\hat{n})$ field into $\gamma_{1,2}(\hat{n})$ yield almost identical results regardless of whether a smoothed mask is applied or not. Finally, the measurements obtained from an octant $\gamma_{1,2}(\hat{n})$ map cutout from the full-sky shear maps exhibit only marginal improvement relative to the other two octant results, suggesting that the main contributor to the noise is sample variance at those scales. We investigate this further in **Test 2**. We comment that on the smallest scales, $\theta < 1$ arcmin, the $\xi_{-}(\theta)$ measurements appear to be noise-dominated. We conjecture that this feature is due to the use of random halo particles as sources, the nearest pixel assignment procedure, and the map resolution of 0.2 arcmin.

Test 2

The second test we perform checks separately the octant conversion procedure by using all 8 octants. We compute two sets of eight measurements, one for each octant. In the first set, we split the full-sky shear maps, $\gamma_{1,2}(\hat{n})$, into eight $\gamma_{1,2}(\hat{n})$ submaps covering an octant of the sky. This provides us the 'idealized' test case, in which the shear maps have been obtained from the full-sky convergence maps. In the second set, we apply the same methodology as we do for the base-resolution simulations: namely, after splitting the convergence
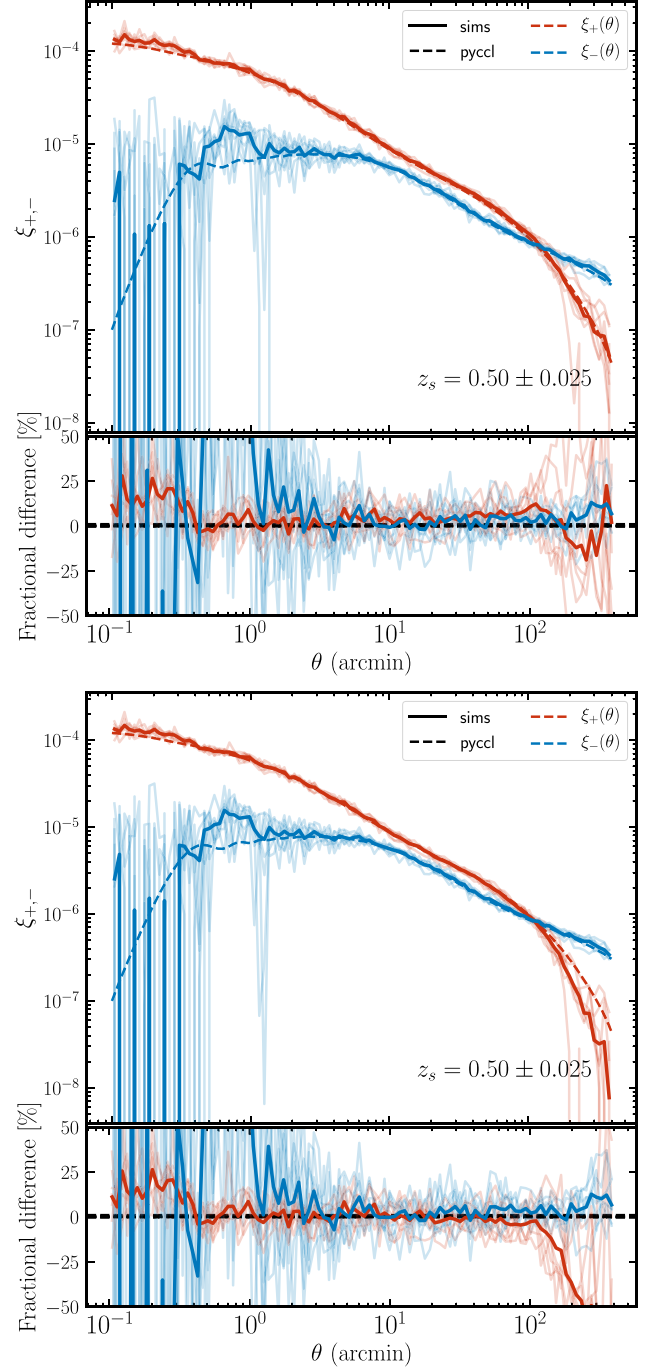

Figure A2. **Test 2**, described in Appendix A, of the shear–shear autocorrelation, $\xi_{\pm}(\theta)$, at source redshift of $z_s = 0.5$, using the AbacusSummit_huge_c000_ph201 simulation. This test serves as a check of the effect of converting an octant $\kappa(\hat{n})$ map into $\gamma_{1,2}(\hat{n})$. The top panel shows the idealized scenario in which the $\gamma_{1,2}(\hat{n})$ map is obtained from the full-sky $\kappa(\hat{n})$ map; then, the full-sky $\gamma_{1,2}(\hat{n})$ map is partitioned into the eight octants. The lower panel corresponds to the case in which the full-sky $\kappa(\hat{n})$ map is first partitioned and then each of the eight octants is converted into $\gamma_{1,2}(\hat{n})$. The ξ_{-} curves appear to be largely unchanged, whereas the ξ_{+} curves are affected beyond $\theta > 100$ arcmin: the average curve in the lower panel displays a cut-off, much like the one in Fig. 4, whereas the average curve in the upper one is more consistent with PYCCL and the full-sky result from Fig. A1. On scales beyond $\theta > 100$, we are dominated by cosmic variance.

map into octants, we apply the appropriate ℓ-filter (see equation 17) to each submap to obtain the shear. We then calculate $\xi_\pm(\theta)$ for the octants in both sets.

In Fig. A2, we see that the ξ_- curves appear to be largely unchanged when comparing set one with set two, whereas the ξ_+ curves differ from each other significantly beyond $\theta > 100$ arcmin. In particular, the average curve in the lower panel displays a cut-off, much like the one in Fig. 4, whereas the average curve in the upper panel is more consistent with PYCCL and the full-sky result from Fig. A1. We conclude that the octant conversion introduces noise along the boundaries that decorrelates the signal on large scales for θ_+, $\theta > 100$, which are also strongly dominated by cosmic variance. We also confirm this via a visual inspection of the difference in the $\gamma_{1,2}(\hat{n})$ maps obtained via both procedures. The source catalogue is constructed using a heavily downsampled halo and particle catalogues, which contributes to the larger overall variance of the signal compared with Fig. 4, as the number density of sources is drastically reduced and the randomly chosen halo particles introduce further noise into the measurement.

APPENDIX B: COMPARISON OF ABACUSSUMMIT POWER SPECTRA TO HALOFIT

In many of the validation plots throughout this paper, we compare the simulation results from ABACUSSUMMIT with PYCCL, which adopts the non-linear matter power spectrum from HALOFIT. However, it is not clear whether HALOFIT provides a good fit to the non-linear clustering on small scales. We address this question in this Appendix by comparing the power spectrum computed from the 25 base-resolution and the two huge-resolution boxes with HALOFIT. The inclusion of the huge-resolution simulations allows us to test the resolution effects of these coarser runs, which as we found in Fig. 3, appear to contribute non-negligibly to the small-scale signal.

Fig. B1 shows the power spectrum of ABACUSSUMMIT and HALOFIT (both total matter and the CDM + baryons) at several different redshifts: $z = 0.1, 0.2, 0.3, 0.4, 0.5, 0.8$, and 1.1. We expect the particles in the ABACUSSUMMIT simulations to be tracers of the CDM + baryons component and therefore, the power spectrum to match the CDM + baryons HALOFIT power spectrum better. In reality, it is hard to say whether that statement holds or not, as the difference between the total matter and the CDM + baryons HALOFIT power spectrum is very small (about 2 per cent for our choice of 0.06 eV neutrino mass). On large scales, however, there are indications that this is likely the case. It appears that the HALOFIT (CDM + baryons) agreement with ABACUSSUMMIT worsens, as we go to lower redshifts, where the ABACUSSUMMIT power spectrum becomes more akin to the total matter signal. This makes sense, as the initial conditions are tuned to reproduce the response of matter in the presence of a smooth neutrino component at $z = 1$, as the redshift of interest for current spectroscopic surveys. For all scales considered, the discrepancies are less than 5 per cent (except for on very large scales, which are dominated by cosmic variance). This is in agreement with the quoted 5 per cent precision error reported for HALOFIT (Takahashi et al. 2012). We comment that at fixed scale, $k = 1\,h\,\text{Mpc}^{-1}$, the huge boxes show larger differences with respect to HALOFIT (matter), which explains the lower panel findings in Fig. 3. The largest k wavemodes shown correspond to the Nyquist frequency for the 2048 grid cells per dimension used in the power spectrum calculation.
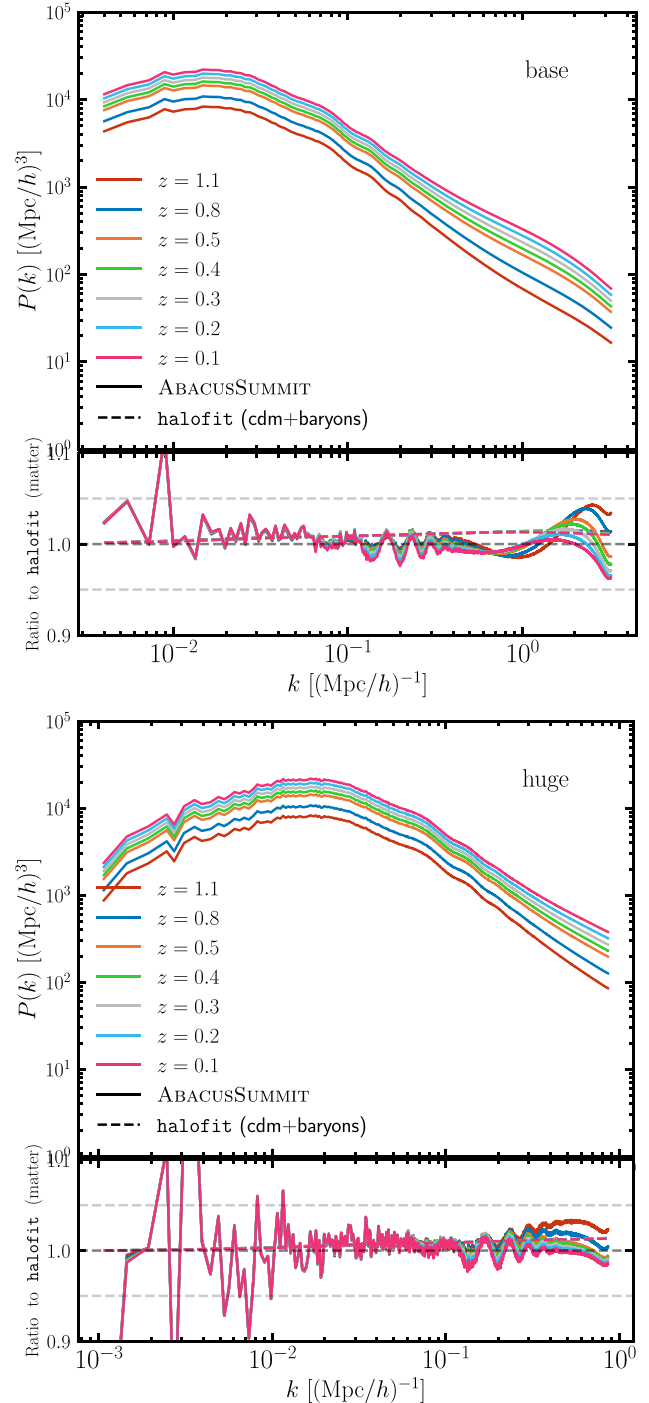

Figure B1. Power spectrum comparison between ABACUSSUMMIT and HALOFIT at various redshifts: $z = 0.1, 0.2, 0.3, 0.4, 0.5, 0.8$, and 1.1. The top panel shows the averaged result for the 25 base-resolution boxes, whereas the bottom one comes from the two huge-resolution simulations. The lower segment of each panel shows the ratio of the ABACUSSUMMIT power spectrum to the total matter power spectrum obtained via HALOFIT, as well as the ratio of the CDM + baryons HALOFIT power to the total matter HALOFIT power. For all scales shown, the discrepancies are less than 5 per cent, in agreement with the quoted 5 per cent error reported for HALOFIT. At fixed scale, $k = 1\,h\,\text{Mpc}^{-1}$, the huge boxes show larger differences with respect to HALOFIT (matter), which explains the lower panel findings in Fig. 3. Note that the upper panel of each segment shows only the simulation results (i.e. without HALOFIT).

[1]*Lawrence Berkeley National Laboratory, 1 Cyclotron Road, Berkeley, CA 94720, USA*

[2]*Department of Physics, University of California, Berkeley, 110 Sproul Hall #5800 Berkeley, CA 94720, USA*

[3]*SLAC National Accelerator Laboratory, Menlo Park, CA 94305, USA*

[4]*Centre for Astrophysics & Supercomputing, Swinburne University of Technology, PO Box 218, Hawthorn, VIC 3122, Australia*

[5]*Center for Astrophysics | Harvard & Smithsonian, 60 Garden Street, Cambridge, MA 02138, USA*

[6]*Physics Department, Boston University, 590 Commonwealth Avenue, Boston, MA 02215, USA*

[7]*Department of Physics & Astronomy, University College London, Gower Street, London WC1E 6BT, UK*

[8]*Instituto de Física, Universidad Nacional Autónoma de México, Cd. de México C.P. 04510, México*

[9]*Departamento de Física, Universidad de los Andes, Cra. 1 No. 18A-10, Edificio Ip, CP 111711 Bogotá, Colombia*

[10]*Department of Physics, The University of Texas at Dallas, Richardson, TX 75080, USA*

[11]*Department of Physics and Astronomy, University of Waterloo, 200 University Ave W, Waterloo, ON N2L 3G1, Canada*

[12]*Aix Marseille Univ, CNRS, CNES, LAM, Marseille 13388, France*

[13]*Department of Physics, Southern Methodist University, 3215 Daniel Avenue, Dallas, TX 75275, USA*

[14]*Perimeter Institute for Theoretical Physics, 31 Caroline St. North, Waterloo, ON N2L 2Y5, Canada*

[15]*Waterloo Centre for Astrophysics, University of Waterloo, 200 University Ave W, Waterloo, ON N2L 3G1, Canada*

[16]*Department of Physics, University of Michigan, Ann Arbor, MI 48109, USA*

[17]*Institut de Física d'Altes Energies (IFAE), The Barcelona Institute of Science and Technology, Campus UAB, E-08193 Bellaterra Barcelona, Spain*

[18]*Institució Catalana de Recerca i Estudis Avançats, Passeig de Lluís Companys, 23, E-08010 Barcelona, Spain*

[19]*National Astronomical Observatories, Chinese Academy of Sciences, A20 Datun Rd., Chaoyang District, Beijing 100012, P. R. China*

[20]*Space Sciences Laboratory, University of California, Berkeley, 7 Gauss Way, Berkeley, CA 94720, USA*

[21]*Institute for Astronomy, University of Edinburgh, Royal Observatory, Blackford Hill, Edinburgh EH9 3HJ, UK*

[22]*Department of Physics, The Ohio State University, Columbus, OH 43210, USA*

[23]*Department of Physics and Astronomy, Sejong University, Seoul 143-747, Republic of Korea*

[24]*School of Mathematics and Physics, University of Queensland, Brisbane, Queensland 4072, Australia*

[25]*Korea Astronomy and Space Science Institute, 776, Daedeokdae-ro, Yuseong-gu, Daejeon 34055, Republic of Korea*

[26]*NSF's NOIRLab, 950 N. Cherry Ave., Tucson, AZ 85719, USA*

[27]*Department of Astronomy and Astrophysics, University of California, Santa Cruz, 1156 High Street, Santa Cruz, CA 95064, USA*

This paper has been typeset from a TeX/LaTeX file prepared by the author.